



DEGREE PROGRAMME IN WIRELESS COMMUNICATIONS ENGINEERING

## **MASTER'S THESIS**

# **Employing VLC Technology for Transmitting Data in Biological Tissue**

Author	Syed Isphandiyar Ali
Supervisor	Marcos Katz
Co Supervisor	Igor Meglinski

March 2019

**Ali Syed Isphandyar. (2019) Employing VLC Technology for Transmitting Data in Biological Tissue.** University of Oulu, Degree Programme in Wireless Communications Engineering. Master's Thesis, 59 p.

## **ABSTRACT**

With the development in wireless communication methods, visible light communication (VLC), a subset of Optical Wireless Communication (OWC) has garnered much attention to employ the technology for a secure short-range wireless communication. We present a feasibility study to determine the performance of VLC in short range wireless transmission of data through biological tissue. VLC is a cost efficient and secure means of transmitting high volume of data wirelessly which can considerably reduce the interference issues caused by electromagnetic pulses and external electric fields.

We present a simple measurement approach based on *Monte Carlo* simulation of photon propagation in tissue to estimate the strength of wireless communication with body implant devices. Using light for communication brings inherent security against unauthorized access of digital data which could be acquired from the low energy body implant devices used for medical diagnosis and other studies.

This thesis discusses the typical components required to establish VLC such as, transmitter, receiver and the channel mediums. Furthermore, two cases of *Monte Carlo* simulation of photon-tissue interaction are studied to determine a possibility if VLC is a suitable substitute to radio frequency (RF) for a more wireless communication with the body implants. The process of theoretical measurement begins with conversion of light intensity into an electrical signal and an estimation of achievable data rate through a complex heterogeneous biological tissue model.

The theoretically achieved data rates of the communication were found to be in the order of megabits per second (Mbps), ensuring a possibility to utilize this technology for short range reliable wireless communication with a wider range and application of implant medical devices. Biophotonics.fi presents a computational simulation of light propagation in different types of computational tissue models comprehensively validated by comparison with the team's practical implementation of the same setup. This simulation is also used in this thesis (5.2.2) to approximate more accurate data rates of communication in case of a practical implementation.

**Key words:** VLC, *Monte Carlo* Simulation, Data Rates, Computation bio-tissue model

## TABLE OF CONTENTS

ABSTRACT .....	2
TABLE OF CONTENTS .....	3
FOREWORD.....	4
LIST OF ABBREVIATIONS AND SYMBOLS.....	5
1. INTRODUCTION .....	8
1.1. Motivation .....	9
1.2. Goal of The Work.....	9
2. VLC TECHNOLOGY .....	11
2.1. Literature Review .....	12
3. VLC SYSTEM DESCRIPTION.....	16
3.1. Driver for Optical Transmitter (LED) .....	16
3.2. Digital Driver.....	17
3.3. Analogue Driver .....	18
3.4. LED for Optical Transmission .....	18
3.4.1. Physical Layer Characteristics.....	20
3.5. Bandwidth Limitation of LED.....	21
3.5.1. Quantum Efficiency.....	22
3.5.2. Biasing and Signal Combining.....	22
3.6. Modulation Techniques .....	23
3.7. Photodetector (Receiver).....	26
4. OPTICAL CHANNELS .....	28
4.1. Indoor Communication Link (Transparent Medium).....	29
4.2. Underwater Communication Link .....	31
4.3. Turbid Medium (Biological Tissue).....	32
5. TISSUE OPTICS .....	33
5.1. Monte Carlo Method of Photon Simulation .....	34
5.2. Photon Simulation in Biological Tissues .....	37
5.2.1. Simulation Results .....	38
5.2.2. Case Study .....	41
6. DISCUSSION AND CONCLUSION.....	44
7. REFERENCES .....	45
8. APPENDICES .....	51

## **FOREWORD**

The topic caught my interest due to its uniqueness in providing cheap, simple and robust alternative to conventional digital communication technology. I would begin with paying my gratitude to almighty Allah who made this research successful, then my parents, siblings, my nieces Manha and Ezzah and my true love Maria for their immense love, support and patience with me in the completion of my degree program. I would also give credit to my late grandmother Kishwar Shah and my late uncle Aamir Shah for the motivation they gave me in their lifetime.

I would especially thank Muhammad Yasir Javed and Hamza Khan for their enormous support both as friends and colleagues. I am indebted to Professor Marcos Katz for his valuable guidance and patience with me throughout this research and I feel honoured to be associated with the Centre for Wireless Communication (CWC) and the University of Oulu. I hope and expect this thesis will provide an effective learning experience and referenced resource for researchers in this topic.

Oulu, Finland March 30, 2019

Syed Asphandiyar Ali

## List of Abbreviations and symbols

MHz	mega hertz
THz	tera hertz
RF	radio frequency
VLC	visible light communication
LED	light emitting diode
MIMO	multiple input multiple output
LTE	long term evolution
5G	fifth generation
AP	access point
CSMA/ CA	carrier sensing multiple access with collision avoidance
ISM	industrial, scientific and medical radio-band
GPS	global positioning system
Wi-Fi	wireless fidelity
Li-Fi	light fidelity
WHO	world health organization
RFI	radio frequency interference
M2M	machine to machine communication
OWC	optical wireless communication
VL	visible light
WDM	wavelength division multiplexing
CSK	colour shift keying
RGB	red, green, blue
ISI	inter symbol interference
OOK	on-off keying
Gbps	gigabits per second
BER	bit error rate
B5G	beyond 5G
PON	passive optical network
FTTH	optical fibre to the home
UWB	ultrawideband
RFID	radio frequency identification
EMI	electromagnetic interference
RSS	received signal strength
AOA	angle of arrival
VLF	very low frequency
SPAD	single photon avalanche diode
PD	photodetector
UOWC	underwater optical wireless communication
NIR	near infrared
DSP	digital signal processing
MOSFET	metal-oxide-semiconductor field-effect transistor

BJT	bipolar junction transistor
CMOS	complimentary metal-oxide
QAM	quadrature amplitude modulation
OFDM	orthogonal frequency division multiplexing
DC	direct current
PAPR	peak to peak power ratio
VPAN	visible light communication private access network
FDM	frequency division multiplexing
CRT	carrier recombination time
EQE	external quantum efficiency
IQE	internal quantum efficiency
AC	alternative current
DC	direct current
IMDD	intensity modulation direct detection
NRZ OOK	non-return to zero on off keying
PWM	pulse width modulation
VPPM	variable pulse position modulation
MSM	multiple sub-carrier modulation
FOV	field of view
LOS	line of sight
NLOS	non-line of sight
SNR	signal to noise ratio
ICI	inter-channel interference
CIR	channel impulse response
UVLC	underwater visible light communication
RTE	radiative transport equation
PHY	physical layer (I, II)
B	blood
S	(haemoglobin oxygen) saturation
W	water volume
F	fat volume
M	melanosome volume
dB	decibel
ACO-OFDM	asymmetrically clipped optical OFDM
ADO-OFDM	asymmetrically clipped DC biased optical OFDM
ASCO-OFDM	asymmetrically and symmetrically clipped optical OFDM
CAP	carrier less amplitude modulation
CIM	colour intensity modulation
CSK	colour shift keying
DCO-OFDM	DC biased OFDM
DFT+OFDM	DC biased OFDM
DHT	discrete Hartley transform
eACO-OFDM	enhanced ACO-OFDM

ePAM-DMT	enhanced PAM-DMT
eU-OFDM	enhanced unipolar OFDM
HACO-OFDM	hybrid asymmetrically clipped optical OFDM
HCM	Hadamard coded modulation
LACO-OFDM	layered ACO-OFDM
Li-Fi	light fidelity
MCM	multicarrier modulation
MM	metameric modulation
M-PAM	M-ary pulse amplitude modulation
M-PPM	M-ary pulse position modulation
OFDM	Orthogonal frequency modulation
OOK	on-off keying
PAM-DMT	pulse amplitude modulation discrete multitone
PM-OFDM	position modulation OFDM
PWM	pulse width modulation
RPO-OFDM	reverse polarity optical OFDM
SCM	single carrier modulation
SEE-OFDM	spectrally and energy efficient OFDM
SFO-OFDM	spectrally factorized OFDM
WPDM	wavelet packet division multiplexing

# 1. INTRODUCTION

The annual run rate for global internet protocol (IP) traffic in 2017 reached 1.5 zettabytes (ZB) and is expected to increase three folds by 2022 i.e. 4.7 ZB. Fixed internet consumption which comes from residential and commercial subscribers is said to form greater part of the traffic than traffic from cell phone towers [1]. Typical indoor wireless communication technologies such as Wi-Fi and Bluetooth have an advantage due to their accessibility through solid non-conductive obstructions. These low power technologies are of great interest to the researchers for futuristic internet of things (IoT) applications but are susceptible to interference caused by other wireless appliances using same frequencies and the cyber security threats that can compromise the confidentiality of the data networks.

The capacity of fifth generation (5G) networks is significantly high due to the heterogeneous structure of the networks comprising of several small cells. Given the battery, latency and accuracy issues with RF transmission in biological tissues, VLC looks like a more suitable option to wirelessly transmit data through tissues. VLC has a broad spectrum (400 THz – 800 THz) which could provide connectivity to massive number of devices, fast and flexible deployment structure and high speed communication. VLC has the capability to address the increasing demand for ubiquitous connectivity and high capacity, overcoming the RF security, latency and electromagnetic interference issues at the same time.

VLC employs Light Emitting Diodes (LEDs) as optical source of transmission, which is already used as preferable source of light in several applications today. LEDs are fast switching sources of light which enables high speed communication with considerably reduced power consumption as opposed to RF components of communication. Unlike radio waves, VLC signals do not penetrate through the walls, which restricts their coverage but eradicates the security vulnerabilities associated with RF networks. The concept of utilizing light for wireless data transmission is adopted in a lot of fields such as vehicle to vehicle communication, underwater communication or other outdoor or Free Space Optics (FSO) based communication. VLC is more suitable for indoor communication for its high bandwidth and easier installation. The easy deployment of VLC is due to the pre-existence of light sources in indoor environments. Besides, VLC is of high interest in electromagnetic sensitive areas such as airplanes, hospitals etc. Besides, inherent security from hacking and the low-cost deployment of VLC setup makes it interesting for research in the exponentially rising market for connected health objects. Short range VLC luminaries are a promising combination for low rate IoT applications as well as gigabit rate wireless networking [68] - [69].

Our research interest is focused around the study and development of very shortrange wireless communication based on VLC for medical applications. The RF based medical devices implanted in body, require considerable amounts of power and produce low efficiency in transmission through the biological tissues. When light is projected over skin, part of it is reflected, part is absorbed, and part is further transmitted. Light radiation reaching viable tissue is partly absorbed, scattered and reflected by the tissue. The amount of light that transverses through the tissue could be detected by an in-vivo medical implant device which could be used for one or multiple purposes. This paves way for endless opportunities in the autonomous clinical applications and other short-range networks applications. Over other advantages, VLC



can serve as a good complement to RF based short range communication for increased coverage and enhanced throughput [2] - [3].

This thesis discusses the problems relating to light transmission in biomedical tissues which are modelled as turbid media and computes the light fluence rate using *Monte Carlo* simulation. *Monte Carlo* simulation deploys a photon transport to assess the wavelength-dependent behaviour of light interacting with turbid tissue models in order to determine if a body implant device can communicate with an external device to establish a non-invasive wireless communication. The future work in this regard will be based on practical implementation of the simulation scenario presented in this thesis.

### 1.1. Motivation

RF based medical implants are getting complex with the passage of time, which makes them a vulnerable target of cybersecurity intrusions. RF based short range communication is more susceptible to hacking providing access to data as sensitive as medical information to an unauthorized person. Light signals do not penetrate through the walls, which gives VLC setup an inherent security. The use of light to transmit digital information to an implant is expected to reduce the power consumption of the process and produce more efficient results. The information can be sensed by a small photodetector embedded in the body implant sensor to receive information at a fast transmission rate. Besides, the work in this thesis is motivated by current environmental considerations focused on mitigating the use of RF radiations and corresponding health risks. Virtually all the wireless communication devices such as mobile phones, radio/ television broadcasting, telecommunication masts, microwave oven, radar, WIFI etc. are common sources of RF radiation. The implantable RF medical devices such as pacemakers, APNEA monitors etc. are susceptible to radiofrequency interference (RFI) which could cause them to malfunction. We suggest the use of VLC especially in the indoor and medical applications for a safer and securer transmission of data.

The use of VLC could reduce potential human and ecosystem health risks associated with RF exposure. LED is expected to overtake incandescent and fluorescent technologies as primary source of lighting in public and private sectors in future. Researchers propose various techniques for a more efficient RF communication with in-vivo medical low power devices. Besides, machine to machine (M2M) communication is on the rise, including the development of smart implant sensors which could communicate with other wireless devices for non-invasive medical diagnosis. For ubiquitous usage of wireless technology and for health care applications can VLC can reduce the signal attenuation problems as well as health risks associated with the use of RF technology. Moreover, VLC in healthcare and diagnosis systems can be made more precise and accurate, within safety limits.

### 1.2. Goal of the Work

The thesis presents a feasibility of using VLC technology for transmitting data in a biological tissue. Light propagation in a multi-layered media gets absorbed, scattered

and reflected. The penetration depth of light through the tissue is altered by its optical properties but is sufficient enough to communicate with a device with a photo-sensor inside the body.

The simulations of photon transport in a complex model of a tissue using *Monte Carlo* method is based on previous works shown in [4], [62] - [63]. We have chosen three wavelengths 532 nm, 770 nm and 1000 nm to study their possible transmission distance in the tissue. The exposure time of light projected on skin is simulated to obtain an estimated fluence rate of the wavelengths. From the resulting fluence rate distributions, a measurement of achievable data rates is presented in the results section. The data rates are convincing enough to consider VLC as a technology to communicate with body implant devices. The future work will be focused on a practical implementation of the computational scenario presented in this thesis.

## 2. VLC TECNOLOGY

Visible light spectrum (370 nm to 780 nm) is the section of electromagnetic spectrum which is visible to human eye. LEDs support high switching rates which is useful for VLC. The fast switching of LEDs can be used to generate a stream of information bits in optical form. VLC aims at utilizing existing electrical and lighting infrastructure in buildings to transmit optical signals over free space which could give some slack to RF technology. In Figure 1. a basic block diagram of a VLC setup is presented

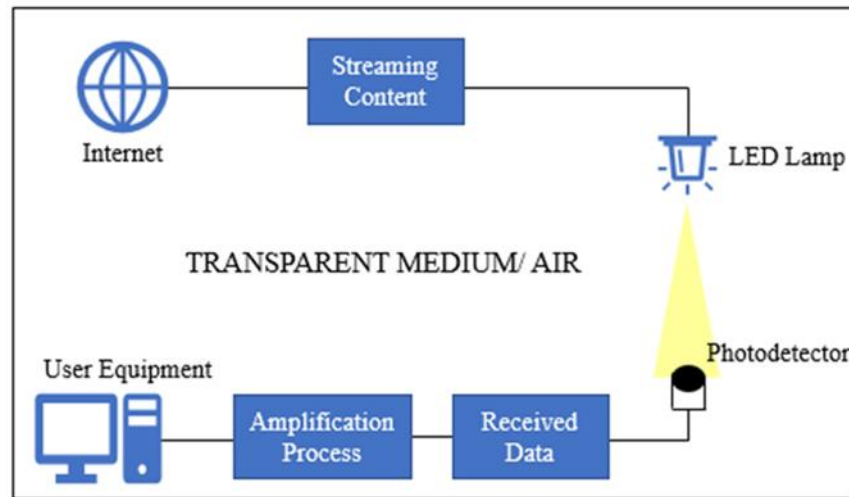


Figure 1. Typical VLC model.

Rapid evolution of LED-based lighting and congestion of RF spectrum occupied by Wi-Fi and cellular radio systems are paving way for VLC in the market. The communication can be established transmitting digital signals using an off-the-shelf LED that can be received by photodiodes that convert light into electric current. The frequency range of visible light is between 430 THz to 790 THz as shown in Figure 2

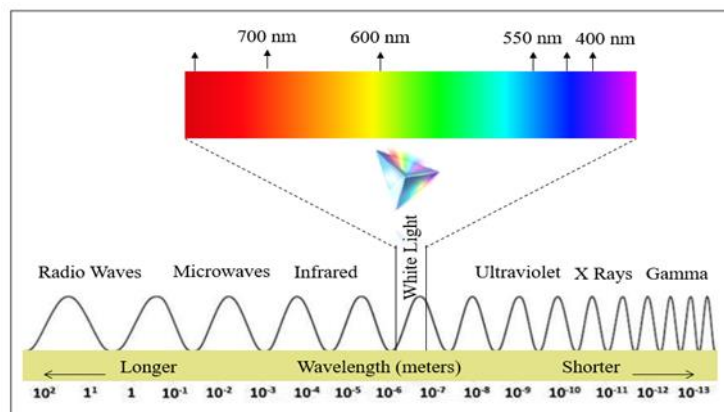


Figure. 2 Visible light spectrum.

Maximum utilization of visible light spectrum could significantly enhance the capacity of digital communication. Colour shift keying (CSK) is an intensity modulation scheme outlined in IEEE 802.15.7, which allows transmission of data

utilizing the colour variation in RGB (red, green, blue) LEDs. The work in [5] reports VLC based commercial transceivers that operate using CSK scheme.

## 2.1. Literature Review

Graham Bell's photo-phone in the year 1880 at Washington D.C., used sunlight as the optical source, a parabolic mirror as a modulation device and a selenium photodetector as a receiver to establish wireless communication over several hundred meters. The communication model can be seen in Figure 3. VLC refers to short-range OWC supported by IEEE 802.15.7 standard established in 2010. IEEE 802.15.7 standard provides flicker free high data rate optical communication with dimming adaptable mechanisms. The task group has developed PHY and MAC layer standards for VLC. The practical and computational implementation of VLC for transmission of wireless data is proposed in various research works [70] - [71].

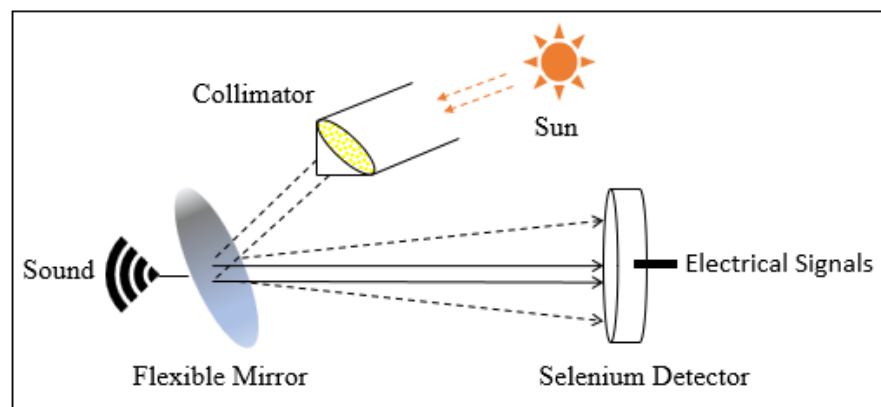


Figure 3. Graham Bell's photo-phone (year 1880).

The first global Li-Fi congress event which took place in the year 2018, aimed to focus on the following applications of VLC.

- VLC based indoor positioning
- LED based communication for internet of things (IoT)
- Optical devices and components for Li-Fi
- Outdoor Li-Fi (smart lighting, transportation, smart city)
- Beyond 5G with VLC /Li-Fi
- Li-Fi for medical applications
- High speed setups and protocols
- Regulation and standardization

Researchers are keen on development of optical broadband sources which could produce homogenous white light with the combination of maximum number of colours (wavelengths) possible. Y. Tanaka proposed utilization of white power of LEDs for optical wireless communication in 2003. The white light LED was composed of three RGB chips capable to achieve a transmission speed of up to 400 Mbps in an indoor

environment [6]. In 2011, Herald Haas established a consortium called Light Fidelity or Li-Fi, with an objective to develop wireless communication using visible light. Li-Fi presented a VLC system in 2013, with a transmission speed of 1.6 Gbps and 2.0 Gbps in 2015 using adaptive bit location technique [7]. Li-Fi's (consortium) research interest include hybrid RF and VLC communication, spatial modulation and interference coordination in wireless networks. Next generation LEDs for lighting in conjunction with internet technology are reported in various studies [8] - [10] where intensity of the light is used to transmit data.

The interference and high latency challenges in RF, make VLC a preferable choice for indoor communication especially after widespread deployment of LEDs for energy efficient illumination infrastructures. In an indoor VLC, inter symbol interference (ISI) due to pulse received from reflection of walls and ceilings is the second limitation after LED's inherent bandwidth limitation. Many techniques have been proposed in different studies, to mitigate ISI and modulation bandwidth of LED. In [11], a symbol encoding technique is used to explore the potential of transmitters mapping in VLC. The proposed technique with on-off keying (OOK) modulation scheme reached data rates up to 2.5 Gbps with a bit error rate (BER) of  $10^{-5}$ . VLC may ensure high data rates with multi-user mobility in indoor environments

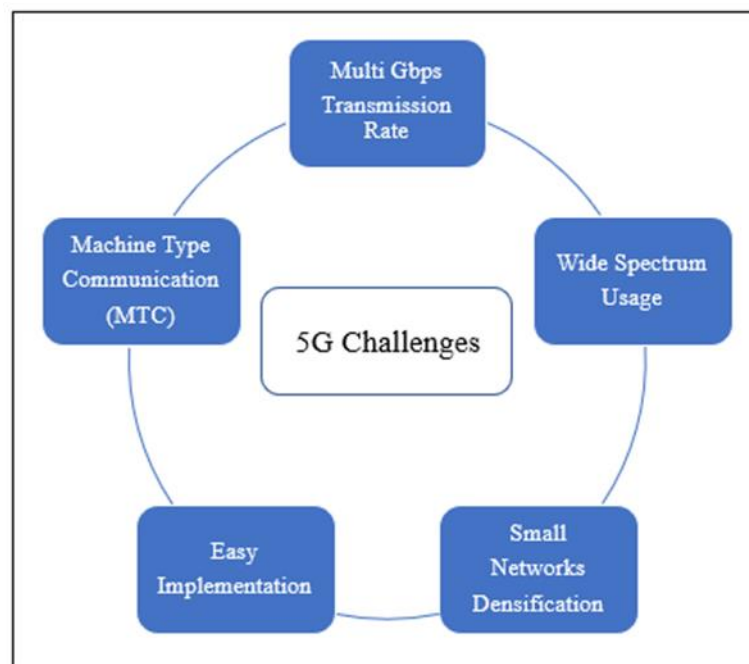


Figure 4. Key technology trends for 5G networks.

5G networks are expected to deploy large numbers of small interconnected cells to provide high capacity communication links. The work in [12] demonstrates gigabits per second (Gbps) and terabits per second (Tbps) communication links using real time wavelength division multiplexing (WDM) PON. The demonstration was made using 8 different wavelengths and a successful speed of 100 Gbps per wavelength. Optical fibre to the home (FTTH) has demonstrated Gbps communication possible in 2000s. This could possibly meet the bandwidth demand for 5G networks based on PON technology. The growing demand of high data rate mobile applications requires deployment of low cost femtocells in the indoors to provide wide coverage. VLC can

be used to off load the congested RF networks in the indoor environments. Indoor communication uses causes higher data traffic compared to outdoor use. VLC could be used as a hybrid to RF technology or complete substitute to provide better spectral efficiency to the users.

Indoor positioning and navigation serves multitudes of mobile devices, but suffers from high attenuation in places like subways, underground malls etc. GPS in RF is widely used in outdoor applications for navigation, but its performance deteriorates in indoor applications due to multipath propagation the attenuation is very high. Indoor localization in VLC is being considered as a promising substitute to GPS in indoor environments. Several techniques such as ultra wideband (UWB), radio frequency identification (RFID) and Bluetooth, used for indoor localization have a slow response rate and EMI is also high. VLC has a strong precision in indoor guidance for human eyes as well as the mobile devices using the same lighting infrastructure. LEDs have been explored for their potential in indoor positioning, based on received signal strength (RSS) [13], angle of arrival (AOA) [14] and VLC hybrid with RF. The work in [15] shows proposed machine learning approaches on the RSS.

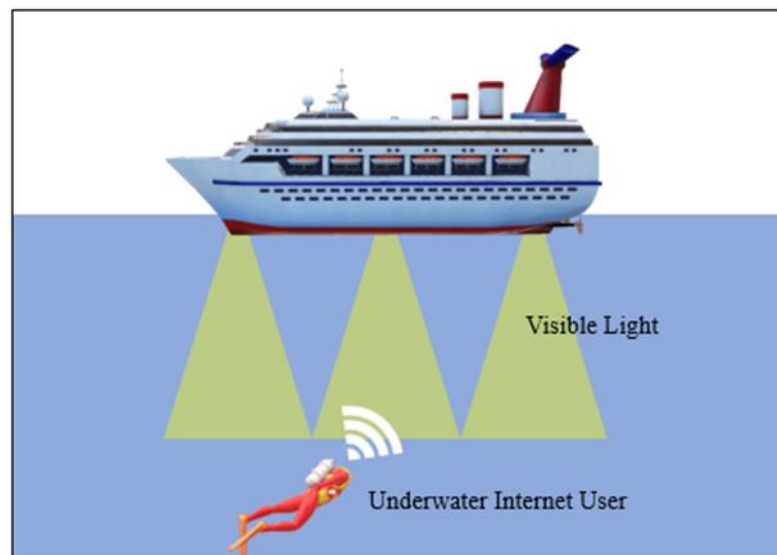


Figure 5. Underwater optical wireless communication.

In addition to outdoor applications, VLC can overcome limitations of subsea applications (submarines, underwater sports, deep sea exploration, subsea oil drilling) where very low frequency VLF radio waves (3-30 KHz) reach depth of approximately 20 meters without the use of additional equipment and lengthy transmission cables. Researchers are devising ways and techniques to establish long range communication underwater using blue wavelength which penetrates deeper in water than other wavelengths. In [16], a long-range underwater wireless communication was proposed. Authors used *Monte Carlo* simulation to model LED as a transmitter, pure sea water as the medium of optical signals propagation and single photon avalanche diode (SPAD) as the receiver. The proposed analytical design established 500 meters deep wireless communication by narrowing down half power angle of LED and using SPAD to improve detection sensitivity.

VLC technology is also evaluated (experimental analysis) for therapeutic diagnosis and other medical applications like Biomedical Sensing Data Transmission,

overcoming health hazards like electromagnetic radiation or interference with precision medical instruments [17]. In [18], visible light is used to communicate with photodetector (PD) over biological tissue as channel medium. The results were found to be more accurate and reliable than RF heart monitoring

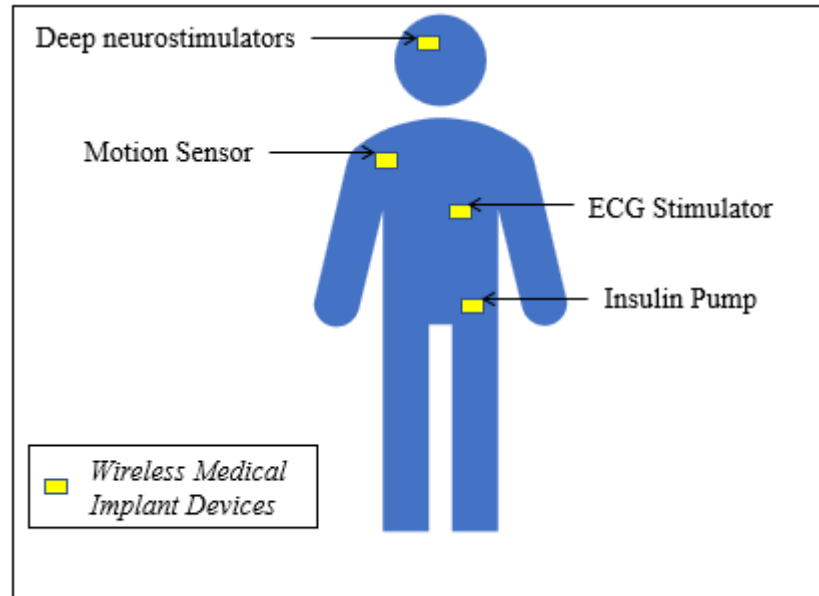


Figure 6. Non-invasive VLC health monitoring model.

Light propagation in any medium is attenuated by absorption and scattering coefficients of that medium. At receiving end, photodetectors are optimized to efficiently generate electrical signal from received light signals. With the combination of photometry and optical properties of the studied material we can introduce and establish accurate, better and safer non-invasive wireless health monitoring applications. The choice of wavelength is application specific, for example 440 nm to 550 nm window which corresponds to the blue and green spectrum shows low attenuation relatively for underwater optical wireless communication (UOWC) for clear water and greener for coastal waters [19] or near infra-red (NIR) is the optical window used in medical (650 nm and 1350 nm) for deeper penetration in biological tissues than other wavelengths.

### 3. VLC SYSTEM DESCRIPTION

LEDs are the optical sources in the VLC transmitter, modulated by a current limiting or voltage limiting driver. A photodetector responds to the incident light on its surface into a directly proportional electrical signal. The responsivity of the photodetector is the measure of the photocurrent at its output in response to the total optical power incident on its surface. The optical medium to be used for communication can be transparent, liquid or layers of biological tissues bearing unique absorption, scattering and reduced scattering coefficients.

Reflection and refraction are design parameters for confined spaces with walls and ceilings. The modulator in Transmitter section transforms data into a series of light pulses (some sequence of 0 and 1) or binary form. The driver carries the modulated frequency of light pulses to the LED. The block diagram of a typical VLC system is shown in Figure 7.

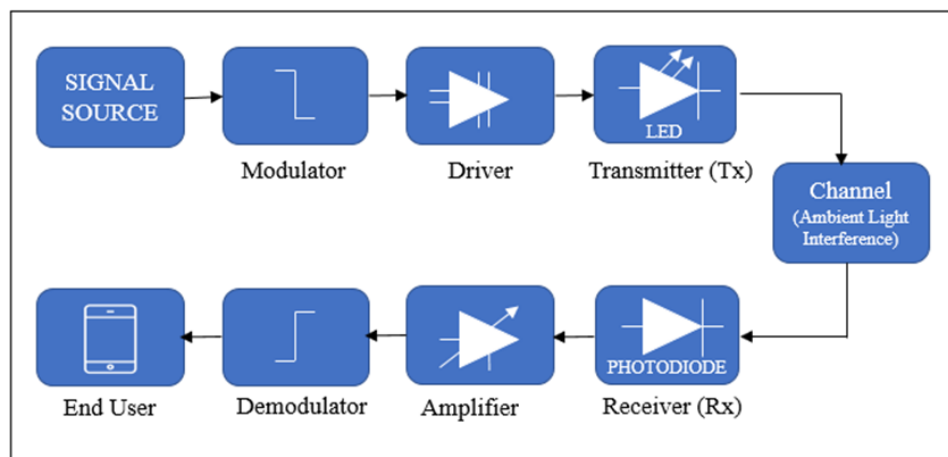


Figure 7. Block diagram of basic VLC system.

Optical detecting patterns in turbid medium such as biological tissue can be improved by digital signal processing (DSP). DSP algorithms are defined to isolate the desired wavelength or wavelengths from the received electromagnetic radiation [20]. The significant parameters of PDs range from their quantum efficiency, responsivity, spectral response range, noise, response time, rise time and gain.

#### 3.1. Driver for Optical Transmitter (LED)

The drivers for LED are classified into digital and analogue mode drivers as shown in Figure 9.



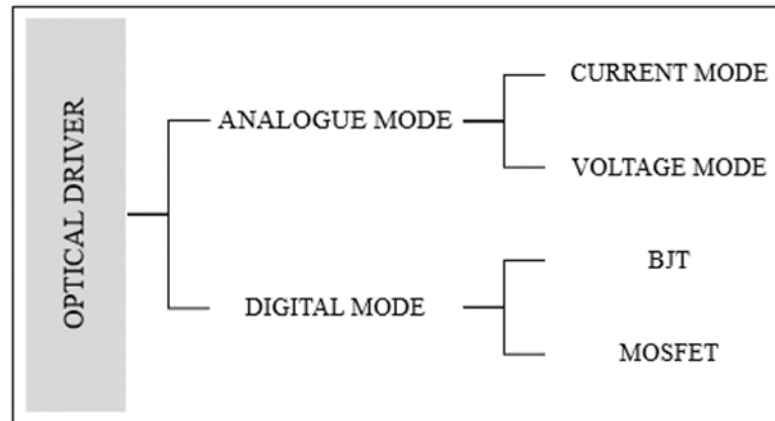


Figure 8. LED driver types.

LEDs are current driven devices and their brightness is proportional to their forward current therefore it is important to design circuits that can control current either by applying voltage which is close to LED's operating point to drive forward current or by using constant current source.

Constant current sources ensure constant LED brightness and experience no current variation due to forward voltage of LED. Drivers that are used for digital data transmission are called Digital or Switch Mode drivers because they operate on using OOK scheme. The switching is done using capacitors or a combination of capacitors in different configurations based on application need. Analog drivers are used for more complex modulation formats.

### 3.2. Digital Driver

Digital or switch mode drivers are used for digital communication transmit data into binary form. MOSFETs are high input impedance, low conduction resistance active devices that have the capability to achieve low power dissipation. LED capacitance has a lower discharging time, typically enough for Mbps communication, external drivers for a faster capacitor discharging time suitable for high speed switching. The metal-oxide-semiconductor field-effect transistor (MOSFET) and bipolar junction transistor (BJT) are two widely considered active devices for digital driver's design. BJT requires a high base current at the input to operate. MOSFETs are preferred over BJT for having low conduction resistance and the ability to handle high currents with low power dissipation. The current mode MOSFETs are used in different combination to reduce discharging time of LED capacitor [21]. Two common types of digital LED drivers that can handle multiple LEDs are shown in Figure 9 (a) and 9 (b)

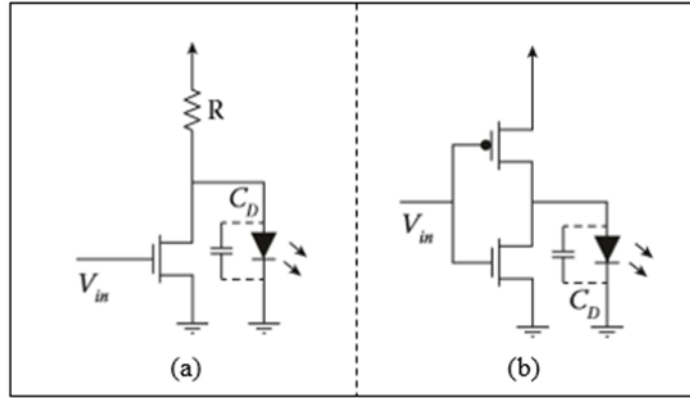


Figure 9. (a) Single transistor inverter (b) CMOS inverter [22].

In circuit 9 (a) current increases in the transistor with the increase in  $V_{in}$  and the capacitor begins to charge. A capacitor in parallel with load (LED) helps to reduce the discharging time. Driver as shown in Figure 9 (b) uses a complimentary metal-oxide (CMOS) inverter configuration with only one transistor active at a time, the lower transistor is used to drain the charge from the capacitor [22] providing high-speed switching.

### 3.3. Analogue Driver

Analog drivers can perform complex modulations of the LED like quadrature amplitude modulation (QAM) and orthogonal frequency division multiplexing (OFDM). Like digital drivers need to be able to switch the LEDs as fast as possible, analogue drivers should be designed to present high linearity. To achieve homogenous modulation as opposed to digital drivers, we will discuss two types of drivers, voltage mode and current mode.

Constant voltage drivers drive the LEDs to produce the signal in the form of voltages and are designed to operate on a fixed direct current (DC) output voltage. LEDs that drive currents less than or equal to the fixed current can be operated to produce signals in the form of voltage variations. The current load value is designed to stay below the fixed DC, for the driver to provide constant voltage output or the driver will overdrive the LED. Constant current drivers are preferred over voltage mode drivers for LEDs linear power to current relation however, the current-voltage non-linearity characteristic of the LED makes it useful for high peak to average power ratio (PAPR) applications [23].

### 3.4. LED for Optical Transmission

A light emitting diode is a semiconductor device which emits visible light in forward bias condition. The device has endless practical applications and has served as one of the important inductions in modern day lighting landscapes. Far field patterns generated by LED define its maximum intensity regions. Most LEDs emit a Lambertian pattern where angular intensity distribution of LED is maximum near  $0^\circ$  and reduces to 50% at half-angle. The far field patterns of LED depend on the different

types of such as Parabolic, Hemispherical or Planar (Lambertian emission) LED. The far field patterns of common LEDs are shown in Figure 10.

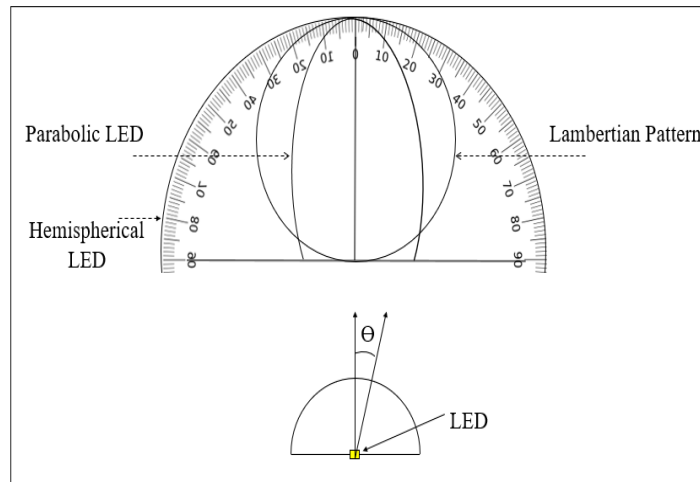


Figure 10. LED far field patterns.

High brightness LED was used in optical fibre signal transmission for the first time in 1976. Gallium nitride was first used in 1986 to produce blue LEDs. The interaction of blue LEDs with phosphor produces white light or by combining red, green and blue colours as shown in Figure 11.

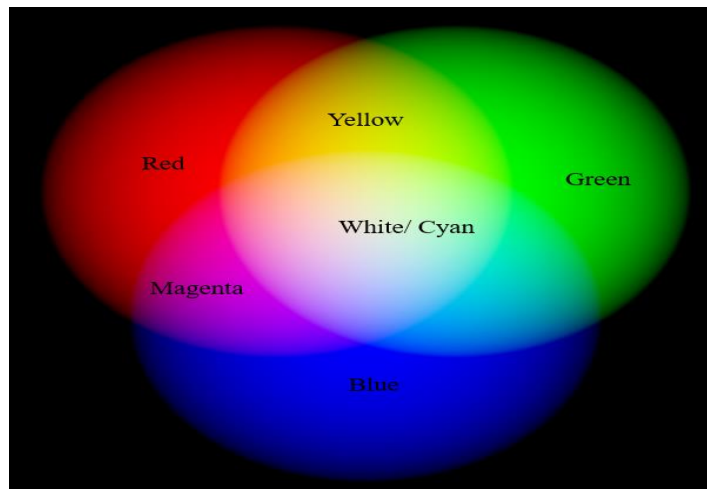


Figure 11. Combination of RGB producing white colour.

LEDs have been used in several devices such as BLU-RAY recording and medical devices since 1993 when Shuji Nakamura invented high brightness blue LED. In 1999, Microsoft introduced an optical input device (IntelliMouse Optical) for personal computers. Optical mouse was equipped with a red LED, instead of a roller ball and a set of sensors to track its movement on a plain surface.

The fast switching capability and diverse colour variation of LED makes it most suitable device for Colour Shift Keying CSK modulation. CSK is an intensity modulation which utilizes the colours as channels to transmit data. The data is transmitted over instantaneous colours of the LED. The bits carrying information are

further processed as binary codes. At receiving end, a lens is used to collect the signals and filter out unnecessary noise.

The use of LED as optical transmitter especially for WPAN has many advantages such as overcoming RF interference, RF restriction in aerospace or hospitals [24], enhanced security under defined coverage and spatial reuse of adjacent cells' bandwidth [25].

### 3.4.1. Physical Layer Characteristics

IEEE 802.15.7 VLC private access network (VPAN) standard applies to network topologies peer-to-peer, star and broadcast as shown in Figure 12.

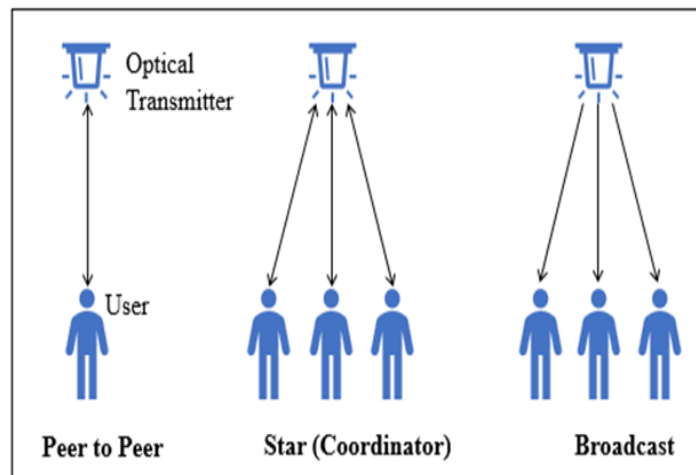


Figure 12. VLC MAC topologies IEEE 802.15.7.

The standard provides

- Access to several hundred THz of free spectrum
- Immunity to EMI and no interference with RF
- Visible security of the network
- Communication augmenting and complementing existing lighting infrastructures.

The physical layers of VLC are occupied by different modulation schemes tailored for application specific purposes. Physical layers I and II use on/ off keying (OOK) where transmission of zero means no carrier is present. Physical layers III use colour shift keying (CSK) technique for multiple input multiple output (MIMO) scenario to provide THz of bandwidth to each user. Therefore, frequency division multiplexing (FDM) remains a good choice for layers with different spectral regions (PHY I and PHY II), which allows them to coexist with each other. Table 1. below shows characteristics of PHY types used in VLC.

Table 1. Physical layers of VLC in standard IEEE 802.15.7 [72]

LAYERS	Operating Range (bps)	Modulation Format	Optimization	Error Correction	Optical Clock Rate
PHY I	11.67 kb/s - 266.6 kb/s	OOK VPPM	Low rate, long distance, outdoor communication	Forward Error Correction (FEC)	$\leq 400$ KHz (High current, low switching time)
PHY II	1.25 Mb/s to 96 Mb/s	OOK VPPM	High rate, indoor, P2P communication	Forward Error Correction	$\leq 120$ MHz (Fast switching for P2P)
PHY III	12 Mb/s to 96 Mb/s	CSK, MIMO (Multiple bits per CSK symbol)	P2P, MIMO	Forward Error Correction	$\leq 24$ MHz

All PHY types in IEEE 802.15.7 are designed to operate in presence of ambient light (light interference) and each layer contains mechanisms for modulating the optical sources. Optical clock rates in PHY types are chosen according to the applications [26].

### 3.5. Bandwidth Limitation of LED

The LED 3 db modulation optical bandwidth is defined by the rate at which the LED power transfer function is reduced by 3 dB. Modulation bandwidth of an optical source is limited by Carrier Recombination Time (CRT). CRT is a finite value of time or the modulation index of a given light emitting diode with respect to a given frequency. If an alternating current (AC) signal is superimposed over an LED, the optical power will decrease with the increase in frequency due to recombination time of the material used in the p-n junction diode. When the current is injected into a p-n junction, recombination takes place and optical power starts building up with respect to a superimposed AC signal. Optical power will reach its maximum value and start decaying at the instant the current is switched down to zero. As the frequency increases, optical power run out of time to reach its maximum because the current is switched off. The modulation index of LED decreases with the increase in frequency. AC current variation or the optical power ( $P_{OPT} \propto i(\omega)$ ) across the LED, reduces with the increase in frequency as seen in (1).

$$i(\omega) = \frac{i_o}{1 + \omega^2 \tau^2}, \quad (1)$$

where  $i_o$  is direct current (DC),  $\omega$  is the AC variation of the optical power and  $\tau$  is recombination time.

Bandwidth is defined where the optical power falls to half of its value.

$$S = \frac{i(\omega)}{i_o} = \frac{1}{2}. \quad (2)$$

The transmission rate of the optical source is dependent on the modulation bandwidth  $F_{3dB}$ , by the following expression:

$$F_{3dB} = \frac{1}{2\pi\tau}, \quad (3)$$

where  $\tau$  is the effective carrier lifetime or recombination time of the source.

RC time constant ( $\tau$ ) is mainly limited by its resistance and junction capacitance and the carriers injected in the device, given by:

$$f = \frac{1}{2\pi RC}, \quad (4)$$

where  $R$  and  $C$  is the resistance and capacitance respectively.

In [27] the enhancement of LEDs maximum transmission speed by a significant number by tuning the carrier lifetime of the LEDs is explained in detail. LEDs with 800 MHz of electrical to optical modulation bandwidths can achieve a transmission rate of Gbps over free-space, using different modulation techniques. In [28], enhancement of 35 GHz of intrinsic modulation bandwidth of a free running semiconductor laser is demonstrated, using injection-locking technique [59].

### 3.5.1. *Quantum Efficiency*

The important performance parameters of LED as an optical source are described briefly in this section. Although the selection of optical source and its properties are highly dependent on the link configuration, channel or medium used for transmission and other factors.

Radiative recombination of electrons and holes is a reverse process of photoionization which triggers production of photons when some voltage is applied across p-n junction. When the electron falls from conduction band to the valence band, photons are emitted. The band gap of the semiconductor and the type of material used in its manufacturing determines the spectral power distribution which is the representation of radiant power emitted by the LED as a function of wavelength. The ratio of photons emitted from the optical source to the electrons required to drive the diode is called External Quantum Efficiency (EQE) whereas, Internal Quantum Efficiency (IQE) of the LED is determined by the ratio of radiation recombination rate to the total recombination rate due to all processes [29].

### 3.5.2. *Biasing and Signal Combining*

Lighting and communication using fast switching LEDs is achieved by combining communication (AC) signal and power using, a bias tee. The communication (AC)

signal is superimposed over DC bias current used to operate LEDs as communication devices. A bias tee comes with different configurations of capacitor and inductor (Figure. 13) where signal components are fed by the capacitor and the biasing is performed by the inductor

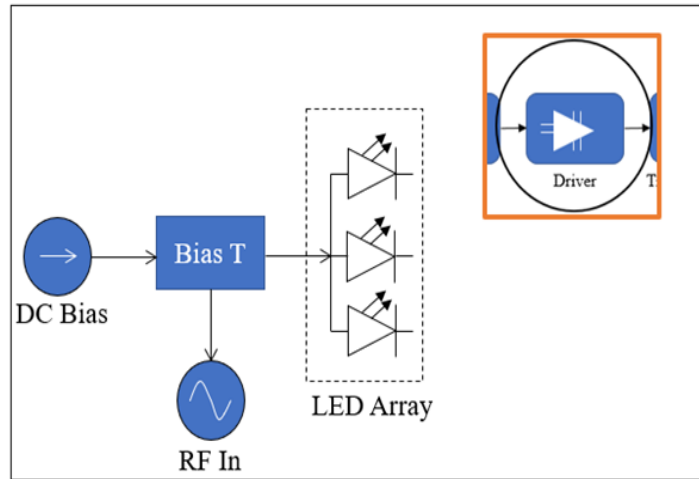


Figure 13. Biasing and signal combining.

In direct modulation technique, the digital ‘On’ is represented as 1 and the ‘Off’ as 0s over a high frequency which is not visible to human eye [30]. In VLC, biasing of the transistor is utilized to combine DC current of the LED with the data for transmission [31].

### 3.6. Modulation Techniques

LEDs are incoherent light sources therefore Intensity Modulation Direct Detection (IMDD) is the only suitable transmission scheme. The phase of the optical carrier cannot be modulated, therefore typical RF modulating schemes are not applicable in VLC. The three modulation schemes standardized by IEEE [12, 24, 79, 80] are OOK, IMDD and CSK. Non-return zero with OOK (NRZ OOK) is the simplest modulation implementation in VLC. NRZ OOK is a binary code where ‘1’ is represented by a light pulse while ‘zero’ means no pulses.

LEDs are current driven devices hence their peak emission wavelength is proportional to variation in forward current. Forward current controls the intensity of light, the reduction of intensity in this process is termed as ‘dimming’ in VLC. Amplitude mode ‘dimming’ method may not be applicable for every VLC application however, pulse width modulation (PWM) technique provides linear dimming scheme. PWM generates a series of current pulses with varying duty cycles in achieving better chromaticity and illumination control. The combination of PWM and variable pulse position modulation (VPPM) is reported to be more effective application for concurrent brightness control and high rate data communication. Variable Pulse Position Modulation VPPM symbols are determined by their position and dimming provided by PWM, assigns duty cycle of each symbol accordingly [22], as shown in Figure (14).

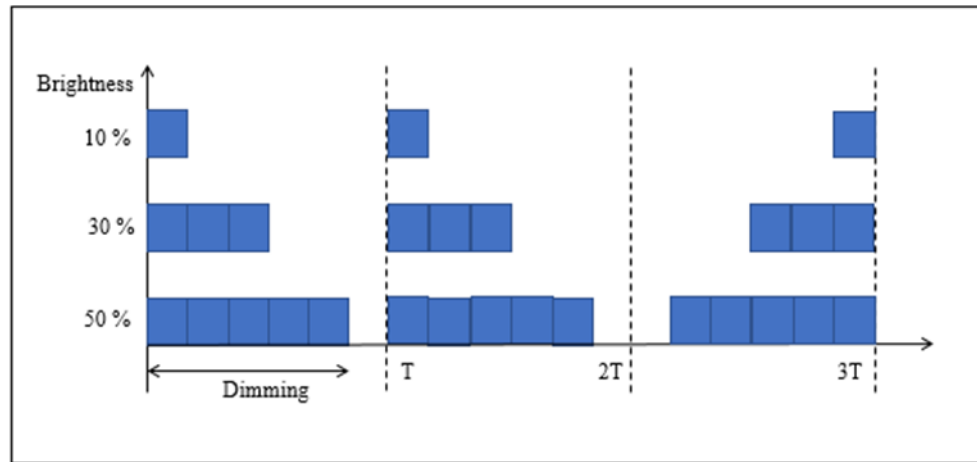


Figure 14. VPPM and PWM mechanism.

Orthogonal frequency division multiplexing (OFDM) is used in multiple sub-carrier modulation (MSM) techniques. MSM techniques are applicable for scenarios where single transmitter provides homogenous transmission of data to several receivers. In MSM, OFDM symbols are modulated onto individual sub-carriers which combine to modulate onto instantaneous power of the transmitter due to orthogonality of sub-carriers. For a high order spectral efficient modulation, VLC employs CSK. CSK is designed to operate with RGB LEDs while maintaining average chromaticity levels. The data is modulated over instantaneous combined RGB radiation such that the source luminous flux remains constant while the chromaticity varies. CSK is preferred over modulation schemes like OOK for their strong isolation with powerline and constant luminous flux [32]. OOK, PPM, OFDM and CSK are compared in the table below, based on different characteristics.

Table 2. Parameters of OOK/ PPM/ OFDM and CSK for VLC

Parameters	OOK	PPM	OFDM	CSK
Bit Rate ( $R_B$ )	$1 \times 10^6$	$1 \times 10^6$	-	20 Mbps
Power Efficiency	Low	High	Moderate	Low
No. of bits/ bits resolution	$1 \times 10^3$	$M = 3$	256 (Number of Symbols)	-
Spectral Efficiency	High	Low	High	Moderate
Samples per symbol	10	250	128 (Number of Symbols)	upto 25 no. of symbols
Bit Duration $T_B$	$1 \times 10^{-6}$	$1 \times 10^{-6}$	-	-
System Complexity	Low	Moderate	High	High
$E_b/ N_0$	1:10	-10:5	[0:1:15]	-
Sampling Time ( $T_s$ )	10	$0.375 \times 10^{-6}$	-	Oversampling rate 25 samples per symbol



Modulation techniques in VLC are designed to provide high spectral efficiency. In VLC, data is modulated over subtle changes in the intensity of light where non-linear distortion needs to be mitigated to improve communication performance. Popular modulation techniques associated with VLC are presented in Figure 15 [33]

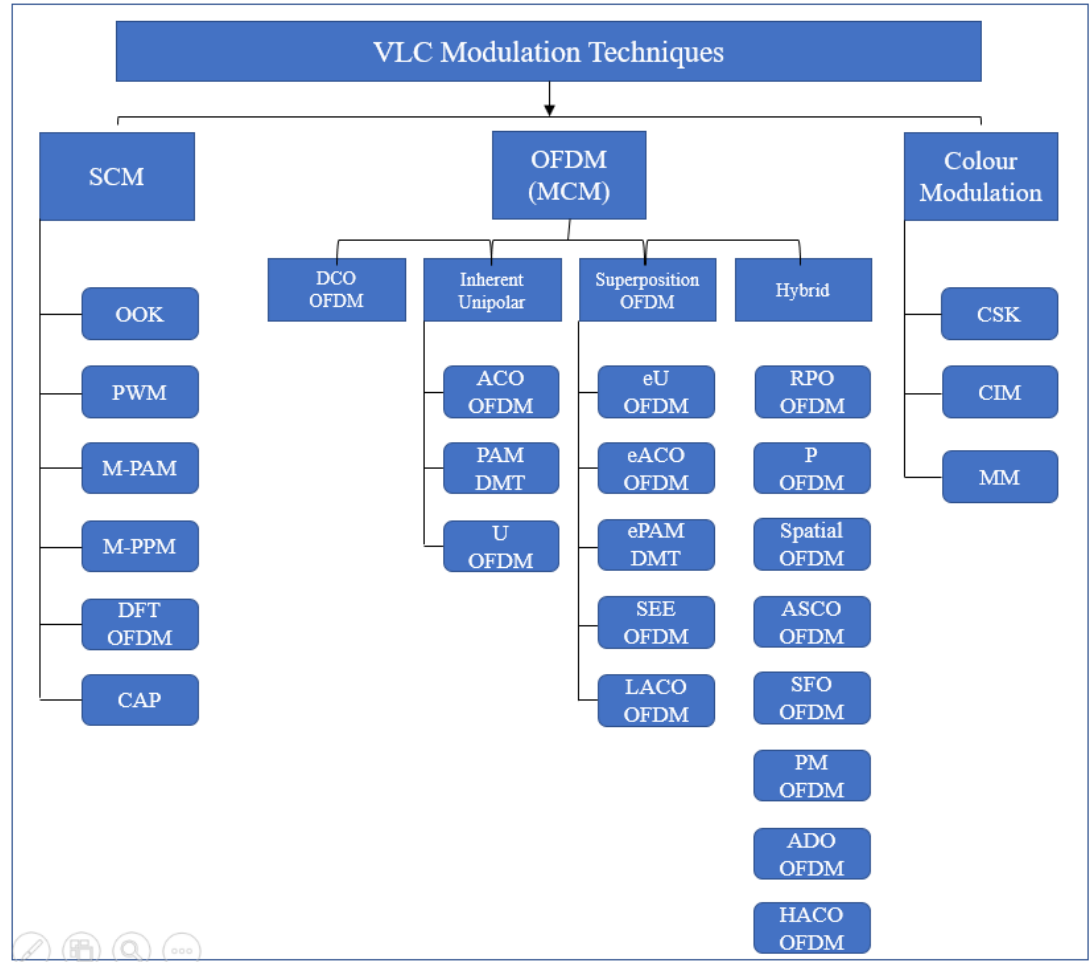


Figure 15. VLC modulation techniques.

ACO-OFDM	asymmetrically clipped optical OFDM
ADO-OFDM	asymmetrically clipped DC biased optical OFDM
ASCO-OFDM	asymmetrically and symmetrically clipped optical OFDM
CAP	carrier less amplitude modulation
CIM	colour intensity modulation
CSK	colour shift keying
DCO-OFDM	DC biased OFDM
DFT+OFDM	DC biased OFDM
DHT	discrete Hartley transform
eACO-OFDM	enhanced ACO-OFDM
ePAM-DMT	enhanced PAM-DMT
eU-OFDM	enhanced unipolar OFDM
HACO-OFDM	hybrid asymmetrically clipped optical OFDM

HCM	Hadamard coded modulation
LACO-OFDM	layered ACO-OFDM
Li-Fi	Light fidelity
MCM	multicarrier modulation
MM	metameric modulation
M-PAM	M-ary pulse amplitude modulation
M-PPM	M-ary pulse position modulation
OFDM	Orthogonal frequency modulation
OOK	on-off keying
PAM-DMT	pulse amplitude modulation discrete multitone
PM-OFDM	position modulation OFDM
PWM	pulse width modulation
RPO-OFDM	reverse polarity optical OFDM
SCM	single carrier modulation
SEE-OFDM	spectrally and energy efficient OFDM
SFO-OFDM	spectrally factorized OFDM
WPDM	wavelet packet division multiplexing

### 3.7. Photodetector (Receiver)

A photodetector works on the principle of detecting photons to produce electrons, above a certain threshold which determines its quantum efficiency. A photodetector can be a vacuum tube e.g. photomultipliers or a semiconductor e.g. photodiodes. The responsivity of the photodetector depends on its capability to produce photocurrent against the amount of optical power incident on its surface.

Typical indoor VLC receiver front-end consist of a PD, pre-amplifier and an electric filter. Choice of optical concentrator, which collects and concentrate distant light source efficiently can be chosen on the factors discussed in detail in [34]. Optical filters enlarge the field of view (FOV), the active receiving area to receive more optical power in NLOS channels. In LOS configuration, the effective receiving area must be kept narrow to avoid ambient light interference, which degrades received SNR. In LOS schemes photodiodes are widely adopted PD for their low cost and high reception bandwidth. For MIMO optical networks image sensors are preferred over photodiodes for their high receiver spatial diversity, which enables them to distinguish between different LED arrays, automatically reducing inter-channel interference (ICI) [35] [36]. Most rooms use multiple illumination sources, which could be employed for MIMO VLC schemes.

#### 3.7.1.1. Performance Parameters

PDs are sensitive to a spectral range of optical wavelengths depending upon their capability to generate photocurrent per unit optical power incident on their surface. The dynamic range or the maximum and minimum detector-optical-power can be limited to avoid damage to the circuitry (e.g. laser induced damage) or their non-linear response in case of a change of bias voltage. The magnitude of dynamic range is

expressed in decibels, which is often an important parameter for a particular application. The ability of a PD to convert light into electrical signal is given by:

$$\eta = \frac{\text{number of electrons produced}}{\text{number of incident photons}}$$

The responsivity  $R_\lambda$  of a PD is dependent on wavelength, defined as the ratio between the photocurrent  $I_{ph}$  produced by the detector and radiant energy  $P$  incident on PD, as shown in (5).

$$R_\lambda = \frac{I_{ph}}{P} \quad (5)$$

For a full-duplex communication between an optical source and a body implant detector when working with strongly divergent beams. To achieve efficient detection of optical signals scattered by the tissues, the photodetector surface area must be large, although with large surface areas, the response of detectors (e.g. photodiodes) gets slow [59].

#### 4. OPTICAL CHANNELS

In optical wireless communication Intensity Modulation (IM) Direct Detection (DD) is a cost effective and most practical modulation technique. The two types of detection in this scheme are either coherent or non-coherent. The former related to detection of phase and amplitude and the latter detects the signal intensity. However, direct detection is preferred over heterodyne detection for its practical simplicity and low cost [32] - [37].

The optical channel properties and equations are briefly explained in [22]. In IMDD the desired signal is modulated onto instantaneous power of carrier wave and detected at the detector side using down conversion technique [38]. Indoor VLC are generally quasi-static because the signals reflected from walls or other reflective objects reach the PD area in a dispersive manner leading to ISI. Pre and post equalization technique shown in [39] to mitigate ISI also increase the LED bandwidth for a NLOS diffuse configuration. Multipath distortion can be modelled as baseband linear impulse response  $h(t)$  for time  $(t)$ . Multipath distortion is high in dispersive or non-LOS channels. Such channels are termed Rayleigh fading channel or its special case Rician fading channel, where the signals arrive at the detector from random paths. The optical signal which reaches the detector's surface is given by:

$$y(t) = R_x x(t) * h(t) + n(t), \quad (6)$$

where  $R$  (A/W) is the PD responsivity,  $x(t)$  and  $h(t)$  are the instantaneous power and  $n(t)$  is the Gaussian or ambient and preamplifier noise and  $*$  denotes the convolution operation.

To analyse the multipath distortion in the channel we use impulse response  $h(t)$  in (7).

$$h(t) = \begin{cases} \frac{2t_0}{t^3 \sin^2(FOV)}, & t_0 \leq t \leq \frac{t_0}{\cos(FOV)}, \\ 0, & elsewhere, \end{cases} \quad (7)$$

where  $t_0$  is the minimum time delay, field of view (FOV) is the active area of the photodetector.

With the increase in transmitter and receiver distance the received power decreases resulting in the decrease in channel DC gain. The signal to noise ratio SNR in OOK is given by:

$$SNR = \frac{R_r^2 H^2(0) \cdot P_t}{R_b N_0}, \quad (8)$$

where  $N_0$  is the noise spectral density,  $R_b$  is the bit rate,  $H$  is the channel DC gain,  $P_t$  is the average optical power transmission, the channel DC gain  $H(0)$  is given by:

$$H(0) = \int_{-\infty}^{\infty} h(t) dt. \quad (9)$$



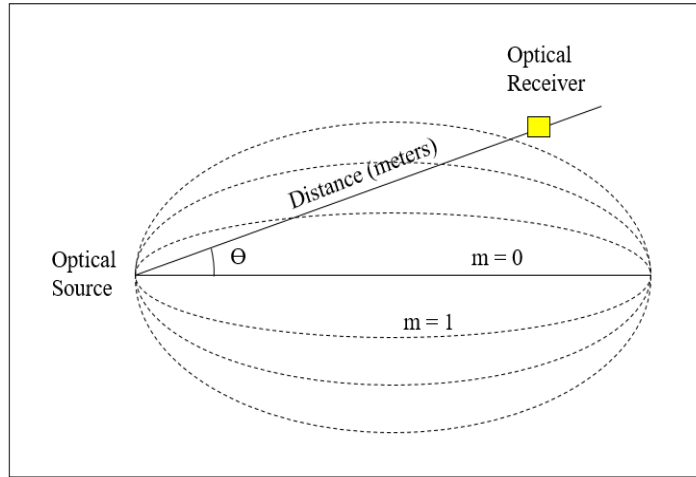


Figure 17. Lambertian order of emission.

The Lambert index  $m$  of an LED is calculated with reference the LED's designed half power beam angle ( $\theta_{\frac{1}{2}}$ ). The relation between  $\theta_{\frac{1}{2}}$  and modulation index  $m$  is as shown in (12).

$$m = \frac{-1}{\ln(\cos \theta_{\frac{1}{2}})}. \quad (12)$$

Light distribution from an optical source is strongest along the center axis and reduces at each sides. The angle at which the intensity reduces to half of the maximum, is known as the beam angle.

White light in LED is produced either by using a combination of RGB LEDs or by using phosphor coating over blue LED. An efficient LED source is preferred for its low power consumption, high luminance, longer life and high switching capabilities. The optical power spectrum produced by LED over a given range of wavelengths is given as follows:

$$P_{opt} = \int_{\lambda L}^{\lambda U} P_t(\lambda) d\lambda, \quad (13)$$

where  $P_t$  is spectrum distribution integrated over  $\lambda L$  and  $\lambda U$ , the lower and upper bound wavelengths.

Light emission from LED is diffusive i.e. light spreads over all directions simultaneously or a directional beam depending on its aperture design. Average optical power transmission  $P_t$  is given by:

$$P_t = \lim_{T \rightarrow \infty} \frac{1}{2T} \int_{-T}^T X(t) dt, \quad (14)$$

where  $X(t)$  is the amplitude of the signal.

The radiation intensity  $R(\phi)$  of an LED as Lambert source of emission can be expressed as:

$$R(\varphi) = \frac{m+1}{2\pi} P_t \cos^m(\varphi), \quad (15)$$

where  $m$  is the modulation or Lambertian index of LED and  $\varphi$  is the angle between direction of beam with respect to 0.

The brightness of LED, illuminance or flux per unit area  $E$  is another important parameter to maintain an equilibrium between brightness and data communication requirement for a room with known dimensions, illuminance  $E$  of LED is given by:

$$E = \frac{d\Phi}{dS} = \frac{I(\theta)}{r^2}, \quad (16)$$

where  $r$  is the distance between transmitter and receiver present in the spatial angle [40].

#### 4.2. Underwater Communication Link

Underwater visible light communication (UVLC), is a great field of interest for the military, underwater sports, deep oil drilling and the scientific community. The main factor that distinguishes UVLC communication from RF communication is its penetration depth in water, since radio waves are strongly absorbed in water. UVLC can be useful underwater in terms of illumination and communication to reach the depths RF cannot reach and to establish communication between multiple transmitters and receivers. In addition, the location of receptors (users) within the range of optical intensity can be accurately identified, tracked and communicated with each other [41] [42]. Underwater OWC channel can be modelled using Beer's Law for a finite distance to predict attenuation loss  $h(L)$  as follows:

$$h(L) = h_c e^{C(\lambda)L}, \quad (17)$$

where  $h_c$  is constant,  $C(\lambda)$  cumulative attenuation or photon extinction coefficient.  $c(\lambda) = a(\lambda) + b(\lambda)$ , where  $a(\lambda)$  and  $b(\lambda)$  are the absorption and scattering coefficients respectively,  $L$  is the communication link distance (meters).

*Monte Carlo* method uses a weighted function of two term exponential approximation to assess multiple scattering events over a finite communication distance.

$$h(L) = a_1 e^{-c_1 L} + a_2 e^{-c_2 L}. \quad (18)$$

The variation of turbidity in oceans or pools is a complex design parameter for a reliable UWOC. Underwater channel turbidity in water is due to microorganisms, bubbles and currents in ocean. The factors that may affect the ability to detect signals accurately underwater are wavelength for transmission, transmitter receiver alignment and variable distance. Light penetration in water results in faster attenuation of longer wavelengths than shorter wavelengths. Longer wavelengths have lower frequencies,

like red light attenuates faster and blue-green wavelength which is 532 nm penetrates deeper in water, the reason why objects appear blue under waters where ambient light is not present. The work in [43] presents a theoretical study for a long distance underwater visible light communication link. The absorption and scattering properties of pure sea water were replicated and a SPAD modelled for improved detectivity of VLC signals. The *Monte Carlo* simulation results showed communication link distance was extended to 500 meters using wavelength close to 532 nm. The skin depth of water for microwaves is barely few meters due to the electric permittivity and dielectric constant of water [44].

### 4.3. Turbid Medium (Biological Tissue)

The absorption of light waves in water is dependent on wavelength [45], compared to air where absorption loss is negligible over a distance compared to water or other turbid mediums like human tissue [46] - [47]. Near infrared window of wavelengths penetrates deeper in human body in contrast with the green and blue wavelength windows [48] - [49].

Optical properties of biological tissues determine the light penetration and the relative energy deposition. Light signals in tissues are governed by absorption  $\mu_a$  ( $\text{cm}^{-1}$ ), scattering (Rayleigh and Mie)  $\mu_s$  ( $\text{cm}^{-1}$ ) and refractive indices. Biological tissues are highly anisotropic i.e. light transmission in a tissue scatters in the forward direction for visible wavelengths [50]. The average value of cosine of the scattering angle  $\theta$  for tissues is  $g \sim 0.9$ , where  $g = \cos \theta$  is the coefficient of anisotropy or the cosine of angle of deflection of the scattered photon. The value of  $g$  ranges between -1 and 1.

$$\begin{cases} -1, \text{totally backward scattering} \\ 0, \text{isotropic scattering} \\ 1, \text{totally forward scattering} \end{cases}$$

The sum of absorption  $\mu_a$  and scattering coefficient  $\mu_s$  is the total attenuation in a turbid medium, given by:

$$\mu_T = \mu_a + \mu_s. \quad (19)$$

Light suffers from high scattering and absorption in tissues [51] due to its structure comprising of absorbing chromophores or primary light absorbing compounds such as blood, water, melanin, fat, yellow pigments etc. The direction of photon after scattering is dependent on the wavelength of the light used and refractive indices of different tissue layers (Elwell & Phil, 1995 [49]).



## 5. TISSUE OPTICS

This section discusses the light tissue interaction presented in (61) as shown in Figure 18. Optical properties of the tissue vary with the path length where part of the light is absorbed, scattered, transmitted and reflected. The mass density fluctuation of various tissue structures (inhomogeneous distribution of blood, bones, cell membranes and other constituents) cause Rayleigh and Mie scattering of light in the tissue. Mie scattering which occurs when the particle is either the same size or larger than the used wavelength, predominates Rayleigh scattering which occurs from particles smaller than the wavelength

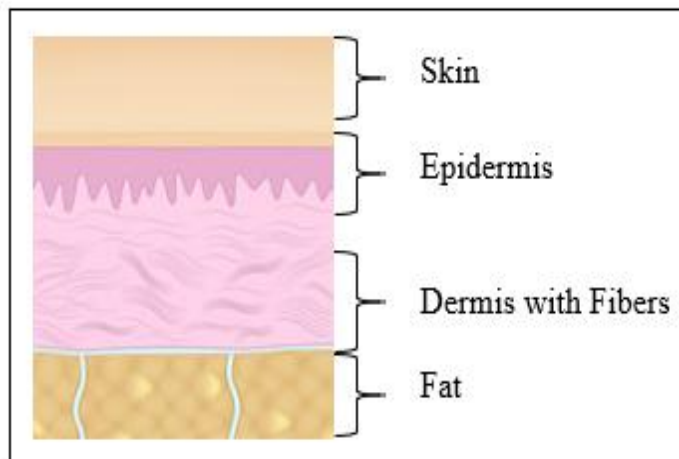


Figure 18. Typical biological tissue structure.

The Rayleigh scattering efficiency ' $k_\lambda$ ' is inversely proportional to the fourth power of the wavelength used in incident light  $k_\lambda \rightarrow 1/\lambda^4$  [52]. When light travels through biological tissues, it scatters in different directions as shown in Figure 19

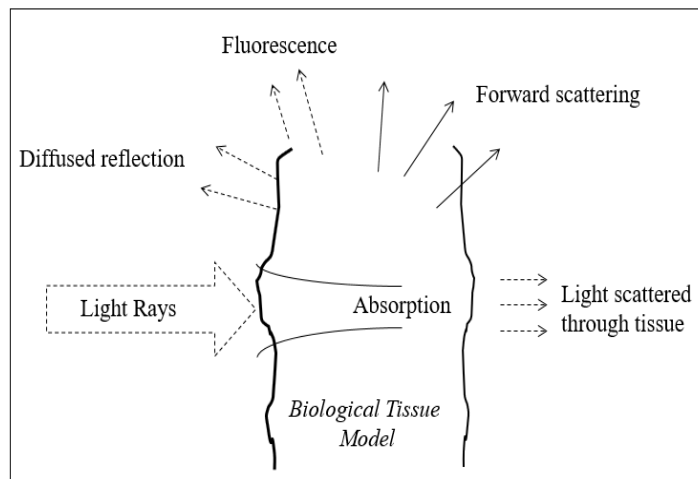


Figure 19. Light beam interaction with bio tissue.

The absorption coefficient as a function of wavelength is given as follows:

$$\mu_a(\lambda) = \sum_i c_i \cdot \mu_{a_i}(\lambda), \quad (20)$$

where,  $c_i$  and  $\mu_{a_i}(\lambda)$  are the concentration level and the specific extinction coefficient of the  $i^{th}$  absorption of the  $i^{th}$  constituent or chromophores of the tissue respectively.

Scattering process is diffusive in tissues due to the liquid-based content like water, lipid and its sub cellular structures like membranes and mitochondria gives rise to diffusive scattering. Light transport in turbid media gets absorbed due to multiple phenomenon which are governed by dimensionless anisotropy factor  $g$ .

$$\mu'_a = \mu_s \cdot (1 - g) [cm^{-1}], \quad (21)$$

where  $\mu'_a$  is the scattering event which occurs when the incident photon advances through incremental length (in meters) and  $\mu_s$  is the reduced scattering coefficient.

The double power reduced scattering function can be written in the form of Rayleigh and Mie scattering as follows.

$$\mu'_s(\lambda) = a_{Ray} \left( \frac{\lambda}{\lambda_{Ref}} \right)^{-4} + a_{Mie} \left( \frac{\lambda}{\lambda_{Ref}} \right)^{-b}, \quad (22)$$

where  $b$  is the dimensionless scatter power,  $\lambda_{Ref}$  is the reference wavelength,  $a_{Ray}$  and  $a_{Mie}$  are Rayleigh and Mie scattering coefficients.

The double power reduced scattering expression as seen in (22) was first used by Mourant et al. (1998) followed by Amelink et al. (2005), Wang et al. (2005), Mirkovic et al. (2009) to model  $\mu'_s$  in terms of scattering probability factors  $a_{Ray}$  and  $a_{Mie}$  and the exponents defining the size of scattering media (Mourant et al. 1997) [53].

### 5.1. Monte Carlo Method of Photon Simulation

*Monte Carlo* is widely used flexible method to simulate light propagation in tissue. The simulation is based on random walks of photon with the tissue layers causing angular deflection of the photons due to scattering. The simulation predicts steady-state light distribution through the multi-layered media which is a close approximation to the real scenario. The scattering of photons in tissue is governed by anisotropy, Rayleigh and Mie scattering. Simple equations for absorption and scattering measurement for a complex tissue are presented from a computer simulation [54] of light transport in a heterogeneous medium. The medium is modelled with varying absorption and scattering properties from Scott Prahl's work in [55]. The absorption property is modelled as:

$$\mu_a = B \cdot S \mu_{a.(Oxygenated)} + B(1 - S) \mu_{a.(Deoxygenated)} + W \cdot \mu_{a.(Water)} + F \mu_{a.(Fat)} + M \mu_{a.(Melanosome)}. \quad (23)$$

The absorption coefficients of the following constituents of tissue model characterize its optical properties.

- B (average blood volume fraction)
- S (haemoglobin Blood, oxygenated and deoxygenated)
- W (water content)
- F (fat content)
- M (melanosome content)

Absorption decreases with the increase in wavelength in the 500 nm – 600 nm range corresponding to melanin and haemoglobin absorption coefficients and further decreasing exponentially from 600 nm to 800 nm. Absorption spectrum, due to melanin concentration in skin varies from darker skin to lighter skin, assuming other chromophores concentrations constant. Melanin volume fraction in epidermis of tissues, as reported by Jacques et al. is 1 – 3% for light skinned, 11 to 16% for Mediterranean skin and 18 to 43% for dark skin [56]. This near infra-red window or therapeutic window 650 nm – 1350 nm has the maximum transmittance through tissues used extensively in medical field such as medical imaging, traumatic brain injuries diagnosis [57], skin and muscle diagnosis in vivo vascular imaging using infra-red II fluorescence [58] allowing quantification of blood velocity in arteries.

The *Monte Carlo* method for simulation of finite number of photons shows distribution of light in a complex tissue comprising of different layers as shown in Figure (20). The spatial distribution of photons in a three-dimensional complex medium with a finite collimated (0.6 cm) beam irradiating a tissue containing a blood vessel is simulated over 532 nm, 770 nm and 1000 nm. An infinite number of photons initially weighted ‘unity’ for computational convenience are launched to propagate through the layers. The photons are injected in the tissue orthogonally at the point of origin of the tissue.

The step size for photon movement is modelled in (24) by sampling the probability distribution of photon in the layers and their angular deflection per scattering event.

$$s = \frac{-\ln(RND)}{\mu_t}, \quad (24)$$

where  $RND$  is a random variable distributed over  $[0,1]$  interval uniformly,  $\mu_t$  known as interaction coefficient, sums up  $\mu_a$  and  $\mu_s$ .

The random variables between 0 and 1 correspond to step size of photon, the deflection and azimuthal angles. MC method is a statistical method of random distribution where every photon can be traced until it exits the medium or is completely absorbed/ extinct. These incremental steps that the large number of photons take are proportional to the computational time. The photon absorbed near the tissues boundary interfaces is decremented in ‘weight’, updated in voxels by (25) and stored in array of T (200, 200, 200) bins.

$$\Delta W = \left( \frac{u_a}{u_t} \right) \cdot W. \quad (25)$$

The decremented weight of photon is deflected by angle  $\theta$  ( $0, \pi$ ) after scattering and the anisotropy is set to 0.9 indicating forward direct scattering, a value typically used

for tissues for visible spectrum. The probability of distribution of photons per scattering event is given as follows:

$$p(\cos\theta) = 1 - \frac{g^2}{2} (1 + g^2 - 2g\cos\theta)^{\frac{3}{2}} \quad (26)$$

Using (26), from Henyey-Greenstein scattering function, we can find out  $\cos(\theta)$  as a function of a random variable as follows:

$$\cos(\theta) = \frac{1}{2g} \left\{ 1 + g^2 - \left[ \frac{1 - g^2}{1 - g + 2g \cdot RND} \right]^2 \right\} \text{ if } g > 0. \quad (27)$$

The azimuthal angle distributed over intervals 0 and  $2\pi$  can be sampled as:

$$\psi = 2\pi RND. \quad (28)$$

The new direction of photon after this process is updated by the following equations:

$$\mu'_x = \frac{\sin(\theta)}{\sqrt{1 - \mu_z^2}} (\mu_x \mu_z \cos \psi - \mu_y \sin \psi) + \mu_x \cos \theta. \quad (29)$$

$$\mu'_y = \frac{\sin(\theta)}{\sqrt{1 - \mu_z^2}} (\mu_y \mu_z \cos \psi + \mu_x \sin \psi) + \mu_y \cos \theta. \quad (30)$$

$$\mu'_z = -\sin \theta \cos \psi \sqrt{1 - \mu_z^2} + \mu_z \cos \theta. \quad (31)$$

The propagation of photon in tissue suffers attenuation from one layer of the tissue, bearing different optical properties to another tissue with different optical properties (32).

The photon step size decreases crossing several layers of tissues until it is small enough to lie in one of the layers, followed by absorption and scattering processes. Photon Package Termination is set to be in process when the photon weight reaches a value too small to be traced. A *Monte Carlo* method called Russian Roulette probabilistically decides photon survival in the medium whereas photon is terminated when the photon weight falls below pre-set threshold weight as  $W = 0.01$ ). A photon can also be partially reflected or transmitted according to some variances of roulette. The results are summarized after enough photons interaction.

The lights bearing wavelengths 532 nm, 770 nm and 1000 nm are separately delivered to the tissue surface as a circular collimated uniform beam of 0.6 cm diameter. The tissue is divided into 200 bins in the x, y and z coordinates. The energy of photons can be determined by (32).

$$E_{ph(\lambda)} = h\nu = \frac{hc}{\lambda}, \quad (32)$$

where,  $E_{ph(\lambda)}$  is the energy of one photon for the given wavelength,  $h = 6.626 * 10^{-34}$  (Plank's constant),  $c = 2.99 * 10^{10} / 1.3$  (Tissue Refractive Index).

## 5.2. Photon Simulation in Biological Tissues

The simulation of light as a point source incident direct over the tissue can be measured using the following equations from the source [59].

$$I_{T(\lambda)} = N_{ph} \cdot E_{ph} \cdot T_{x(area)}, \quad (33)$$

where  $N_{ph}$  is the total number of launched photons and transmission diameter is set to be  $T_{x(area)} = 0.6$  cm.

The received intensity  $I_R$  measurement is carried out at four different depths of the tissue as shown in equation (11) rewritten as follows.

$$I_R = I_T^{(-\mu_T \cdot d)}, \quad (34)$$

where  $\mu_T$  is sum total of absorption  $\mu_a$  and scattering coefficients  $\mu_s$  of the tissue layers.

The simulation was carried out using 532 nm, 770 nm and 1000 nm wavelengths separately. The simulation uses the absorption, scattering and anisotropy values from Scott Prahl's work [55]. The wavelength corresponding optical properties for the three wavelengths are presented in Tables 3, 4 and 5 respectively.

Table 3.  $\mu_a$ ,  $\mu_s$  and anisotropy of the tissue model using wavelength 532nm

Parameter	$\mu_a$ (cm <sup>-1</sup> )	$\mu_s$ (cm <sup>-1</sup> )	$\mu_T$ (cm <sup>-1</sup> )
Water	0.0004	10	10.0004
Blood	230.542	94	324.54
Epidermis	0.4585	356.5	356.958
Dermis	16.572	375.9	374.472

Table 4.  $\mu_a$ ,  $\mu_s$  and anisotropy of the tissue model using wavelength 770nm

Parameter	$\mu_a$ (cm <sup>-1</sup> )	$\mu_s$ (cm <sup>-1</sup> )	$\mu_T$ (cm <sup>-1</sup> )
Water	0.024	10	10.024
Blood	4.389	64.9	69.289
Epidermis	0.0252	151.4	151.425
Dermis	4.8561	259.7	264.556

Table 5.  $\mu_a$ ,  $\mu_s$  and anisotropy of the tissue model using wavelength 1000nm

Parameter	$\mu_a$ (cm <sup>-1</sup> )	$\mu_s$ (cm <sup>-1</sup> )	$\mu_T$ (cm <sup>-1</sup> )
Water	0.360	10	10.360
Blood	4.731	50	54.731
Epidermis	0.242	97	97.242
Dermis	2.29	200	202.296

The optical properties determine the fluence rate of photons in the turbid medium which is further used to determine the amount of intensity present through the depths of the tissue model. The wavelength dependent photon fluence rate shows the total number of photons incident from all the directions. We will use a separate simulation (see appendices 1 and 2) to measure the total number of photons incident on a photodetector model of a specific cross-sectional area of detection which is known as spherical irradiance.

### 5.2.1. Simulation Results

The fluence rate measurements are carried out using previous work [60] on *Monte Carlo* simulation of photons in a complex tissue. The relationship between fluence rate and light intensity is of major importance to this study. The fluence rate data obtained from *Monte Carlo* simulation can be used to find out light intensity as shown in the following equation taken from [61].

$$F = I_R \cdot \tau_p, \quad (35)$$

where  $F$  is the fluence rate,  $I_R$  denotes the intensity of light and  $\tau_p$  is the pulse width or exposure time.

The fluence rate as shown in (36) was used (see Appendix 1) to measure light intensity at different depths of the tissue as presented in Figure 20

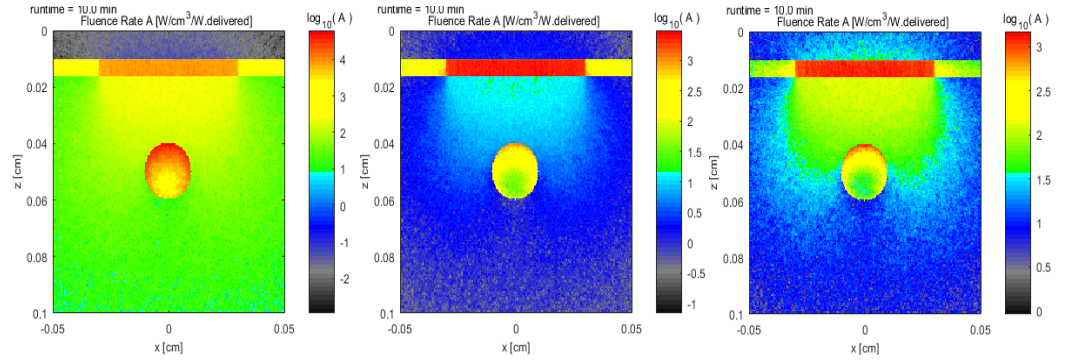


Figure 20. Fluence rates of 532 nm, 770 nm and 1000 nm.

The complex tissue medium is comprised of five layers of tissues with unique optical properties. Light intensity was measured at four variable depths of the tissue. The pulse width or exposure time  $\tau_p$  was set to be an incremental value between 1 picosecond and 10 picoseconds. The intensity of light incident on the photodetector is assumed to be at these four different depths. The received optical power can be measured using (37).

$$P_{o(\lambda)} = I_R \cdot Area_R, \quad (36)$$

where  $P_{o(\lambda)}$  is the received optical power for the given wavelength and  $Area_R$  is the surface area of the photodetector.

The photocurrent  $I_{PH}$  generated by the PD is given by:

$$I_{PH} = R_A \cdot P_{o(\lambda)}, \quad (37)$$

where  $R_A$  is the responsivity of the photodetector set to be 0.46.

To measure signal to noise ratio (SNR) at depths of the tissue, three different kinds of noise are considered in optical devices shot noise, Johnson noise and dark current of the photodetector. For computational convenience, only the intrinsic noise of the photodetector i.e. the shot noise is used in this simulation given by:

$$i_n = \sqrt{2 \cdot e \cdot (I_D + I_{PH}) \cdot B}, \quad (38)$$

where  $e$  is the charge ( $1.602 \times 10^{-19}$ ) of one electron,  $I_D$  is the dark current set to be  $0.03 \times 10^{-9}$  and the bandwidth  $B$  of the photodetector channel is  $10^6$  Hz.

The SNR of the communication can found using (40).

$$SNR = \frac{I_{PH}^2}{i_n^2}. \quad (39)$$

We used Shannon's capacity formula to find out the binary bits of possible communication between the fixed source of transmission projected on the tissue and the photodetector at any given depth.

$$C = B \log_2(1 + SNR). \quad (40)$$

To achieve maximum achievable data rates of the communication between fixed source and the photodetector, it is vital to use the same bandwidth that we used in equation (39) i.e.  $10^6$  Hz. The two-dimensional plots of the simulation are presented in Figures 21, 22 and 23

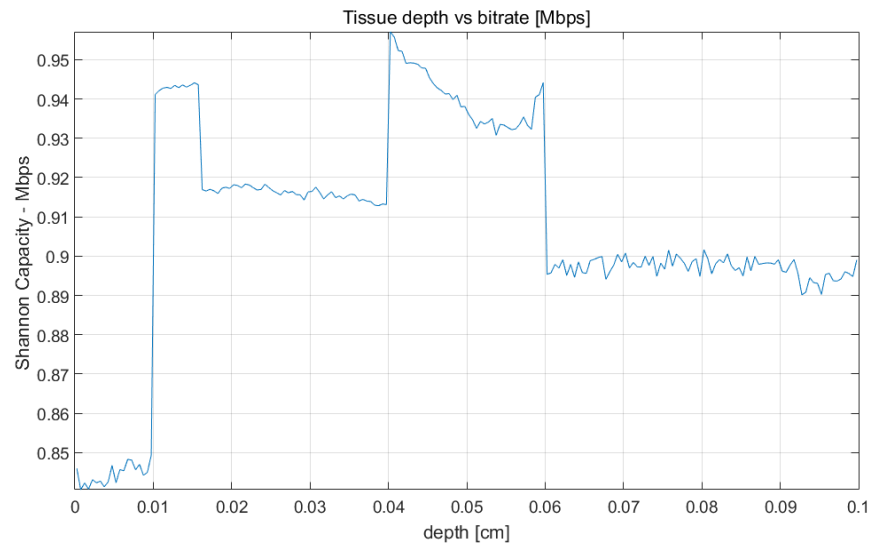


Figure. 21 Achievable data rates using 532 nm wavelength.

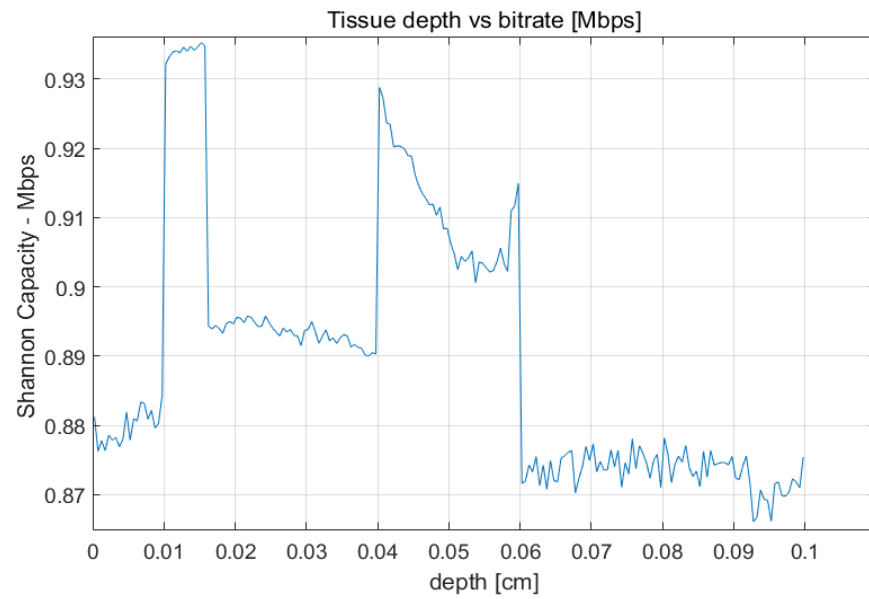


Figure. 22 Achievable data rates using 770 nm wavelength.

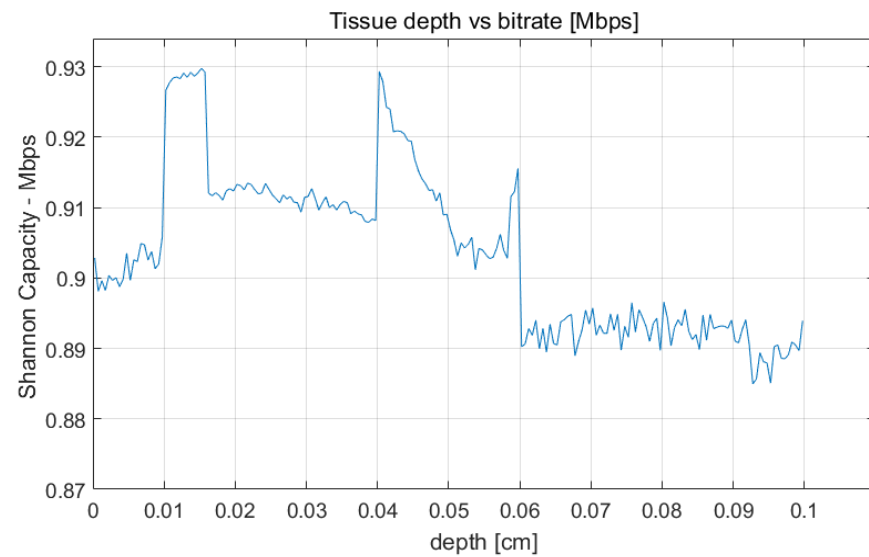


Figure. 23 Achievable data rates using 1000 nm wavelength.

Figure 20 represents the fluence rates measured using 532 nm, 770 nm and 1000 nm wavelengths projected on the tissue model. Figure 20 is a readable file, (see Appendix 1) uploaded in the simulation program to measure achievable data rates of a possible communication between the light source and photodetector. The achievable bit rate measurements as can be seen in Figures 21, 22 and 23 represent the intensity of light penetrating through the depths (y-axes) of tissue models shown in Figure 20.

The peak observed between depths 0.01 and 0.02 is due to water layer above skin, which has higher permittivity for light than the skin, similarly the peak between 0.04



and 0.06 is due to higher permittivity of light through blood artery as shown in Figure 20. A slight decrease in data rates is observed as the light transverses through the tissue models. The initial data rates of the communication using 1000 nm and 770 nm wavelengths are greater than 532 nm, although 532 nm wavelength seems to support a consistent connectivity compared to 770 nm and 1000 nm wavelengths. The maximum achievable data rates possible according to the simulation of photon fluence distribution of 1000 nm wavelength in the simulation is close to 0.9 Mbps. In the next section, a separate photon fluence distribution simulation is studied to compare the data rate measurements in obtained in this section.

### 5.2.2. Case Study

Another case based on the work of Meglinski et al. [62] - [63] is discussed in this section to find out the difference between the two simulation works. In this simulation work [64] a high dynamic range optical to near infra-red transmission measurements is done on various human body parts. The spectral range of 650 nm to 950 nm through various parts of human body are correlated with *Monte Carlo* simulation using CIELAB colour space, which expresses colours as three unique numerical values as 'L', 'A' and 'B'. In this scheme L is for lightness, whereas 'A' and 'B' denote the green-red and blue-yellow colour components. The newly developed technique will help acquire more accurate results for in-vivo optical diagnostics since the chromacity coordinates are in complete agreement with the experimentally measured spectra.

The experimental setup comprised of spectroscopy employed high energy picosecond laser pulses and a large area photonic crystal fiber. The optical properties and the colour of tissue used in the simulation were based on the inhomogeneous spatial distribution of blood, water, melanin, the degree of blood oxygenation and the haematocrit index based on their previous work in [65], [66] - [67].

The tissue was irradiated with a high intensity white light continuum between 650 nm and 950 nm. The light was collected at the other side of the body using a 0.6 mm<sup>2</sup> multimode optical fibre cable. The other end of the receiving fibre opening was connected with an imaging spectrometer. The fluence rate application in the simulation is a sample estimator of fluence rate distribution. The optical properties absorption, scattering, anisotropy, index and thickness of tissue were set as shown in the Table 6 were used for the 633 nm wavelength of light.

Table 6. Simulation parameters for fluence rate estimation

Layer #	Layer Name	$\mu_s$ [mm <sup>-1</sup> ]	$\mu_a$ [mm <sup>-1</sup> ]	g	n	d	
1	<a href="#">Stratum corneum</a>	<a href="#">80.0</a>	<a href="#">0.2</a>	<a href="#">0.86</a>	<a href="#">1.53</a>	<a href="#">20.0</a>	<a href="#">+ x</a>
2	<a href="#">Living epidermis</a>	<a href="#">45.0</a>	<a href="#">0.1</a>	<a href="#">0.8</a>	<a href="#">1.34</a>	<a href="#">80.0</a>	<a href="#">+ x</a>
3	<a href="#">Papillary dermis</a>	<a href="#">30.0</a>	<a href="#">0.1</a>	<a href="#">0.9</a>	<a href="#">1.4</a>	<a href="#">100.0</a>	<a href="#">+ x</a>
4	<a href="#">Upper blood net dermis</a>	<a href="#">35.0</a>	<a href="#">0.1</a>	<a href="#">0.95</a>	<a href="#">1.39</a>	<a href="#">80.0</a>	<a href="#">+ x</a>
5	<a href="#">Reticular dermis</a>	<a href="#">25.0</a>	<a href="#">0.1</a>	<a href="#">0.8</a>	<a href="#">1.4</a>	<a href="#">1620.0</a>	<a href="#">+ x</a>
6	<a href="#">Deep blood net dermis</a>	<a href="#">30.0</a>	<a href="#">0.1</a>	<a href="#">0.95</a>	<a href="#">1.38</a>	<a href="#">200.0</a>	<a href="#">+ x</a>
7	<a href="#">Subcutaneous fat</a>	<a href="#">5.0</a>	<a href="#">0.1</a>	<a href="#">0.75</a>	<a href="#">1.44</a>	<a href="#">5900.0</a>	<a href="#">+ x</a>

The fluence rate application performs the simulation of light into the complex composite tissue structure and produces a fluence rate as shown in Figure 24

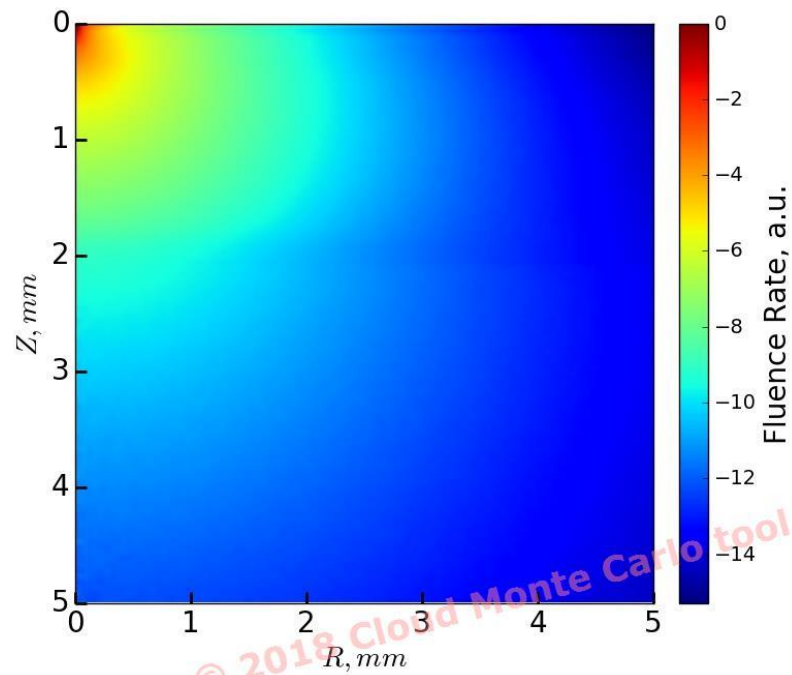


Figure 24. Fluence rate measurement for 633 nm wavelength ([www.biophotonics.fi](http://www.biophotonics.fi))

Figure 24 is a readable file (see Appendix 2), used to find out the numerical values of fluence rate distribution across the tissue medium. Light intensity was measured using (36) and further converted into electrical signals using (39)

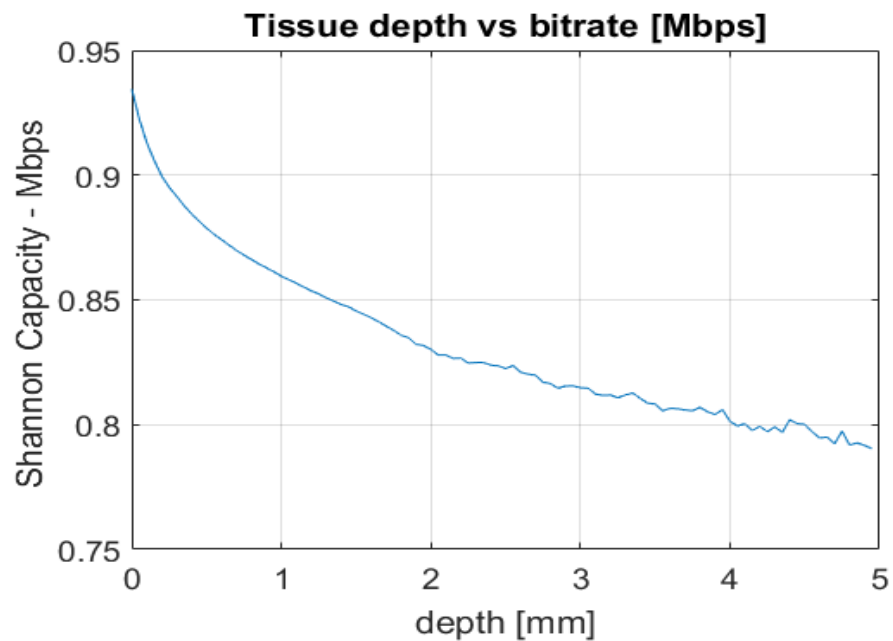


Figure 25. Achievable data rate using 633 nm wavelength ([www.biophotonics.fi](http://www.biophotonics.fi))

The two different case studies presented in 5.2.1 and 5.2.2 are simulated over tissues of different optical properties. However, the results in Figure 25 are more accurate and realistic based on the fact the optical properties used as reference for this simulation are recently updated, however the simulation in 5.2.1 was based on optical properties of tissues updated in 1996 [55]. The results from 5.2.1 suggest the use of near infrared wavelengths for a wireless communication using visible light while the results in 5.2.2 are obtained using 633 nm wavelength. The theoretically achievable data rates in Figure 25 are close to 0.95 Mbps. The data rates decrease as the light transverses through the tissue model, but a strong connectivity seems theoretically possible. The future work intends to present an investigation of an implantable photodetector exposed to an optical transmitter to compare the results in Figure 25. The objective of the demonstration is to assess the possibility of VLC setup between an implant photodetector an optical source in comparison to the theoretical study presented in this thesis.

## 6. DISCUSSION AND CONCLUSION

The results from the simulations are based on two different tissue models. A *Monte Carlo* simulation was tested to produce corresponding fluence rates for different (532 nm, 770 nm and 1000 nm) wavelengths, which was mathematically transformed into detectable light intensity in the tissue model. The intensity of light observed using 1000 nm wavelength was greater than that of 770 nm and the intensity of 770 nm was observed to be greater than 532 nm. Since the thickness of the tissue model was 0.1 cms, the difference in the penetration depths was not found to be too noticeable. Light intensity was measured from the vertex of optical source towards the boundary of the tissue along y-axis. An optical detector produces electrical signal proportional to the received optical signal, however the intrinsic noise of the detector significantly impacts the SNR of the communication. The active area and bandwidth of the detector model was kept constant for both the simulations for a comparative output.

The results reveal that wireless communication between a static light source and a photodetector is possible based on the achievable data rates shown in Figures 21, 22, 23 and 25. The range for such a short-range wireless communication seems slightly different for different wavelengths (532 nm, 633 nm, 770 nm and 1000 nm) as perceived from the results in this thesis, however this flexibility allows us to transmit multiple data streams to an implantable device, using a single homogenous light source typically an LED. The optical properties of tissue model studied in section 5.2.2 was completely different from the first tissue model used in section 5.2.1 furthermore, the structure of both the tissue models was also different. However, the results in both the simulations were observed to be close to each other for the same detector model.

The study reveals a possibility of wireless communication in the order of Mbps, supporting larger amounts of data transmission to the lifesaving and life sustaining prosthetic implantable devices as well as microchip implants used for identification, like radio frequency identification (RFID) implant devices. Based on studies and channel performance measurements in this thesis, VLC technology is strongly suggested for high speed high capacity wireless communication with implant device(s) for its low-cost implementation, safety from RF exposure, less complex circuitry design, immunity from RF interference and high security against hacking of sensitive medical and personal information.

## 7. REFERENCES

- [1] Cisco, V.N.I., 2017. Cisco Visual Networking Index: Forecast and Methodology 2016--2021. (2017) (Accessed 10 May 2018).
- [2] Chowdhury, H., Ashraf, I. and Katz, M., 2013, August. Energy-efficient connectivity in hybrid radio-optical wireless systems. In *Wireless Communication Systems (ISWCS 2013)*, Proceedings of the Tenth International Symposium on (pp. 1-5). VDE.
- [3] Chowdhury, H. and Katz, M., 2013, November. Cooperative multihop connectivity performance in visible light communications. In *Wireless Days (WD)*, 2013 IFIP (pp. 1-4). IEEE.
- [4] Flock, S.T., Wilson, B.C. and Patterson, M.S., 1989. *Monte Carlo* modeling of light propagation in highly scattering tissues. II. Comparison with measurements in phantoms. *IEEE Transactions on Biomedical Engineering*, 36(12), pp.1169-1173.
- [5] Ahn, K.I. and Kwon, J.K., 2012. Colour intensity modulation for multicoloured visible light communications. *IEEE Photonics Technology Letters*, 24(24), pp.2254-2257.
- [6] Tanaka, Y., Komine, T., Haruyama, S. and Nakagawa, M., 2003. Indoor visible light data transmission system utilizing white LED lights. *IEICE transactions on communications*, 86(8), pp.2440-2454.
- [7] Huang, X., Chen, S., Wang, Z., Shi, J., Wang, Y., Xiao, J. and Chi, N., 2015. 2.0-Gbps visible light link based on adaptive bit allocation OFDM of a single phosphorescent white LED. *IEEE Photonics Journal*, 7(5), pp.1-8.
- [8] Komine, T., Lee, J.H., Haruyama, S. and Nakagawa, M., 2009. Adaptive equalization system for visible light wireless communication utilizing multiple white LED lighting equipment. *IEEE Transactions on Wireless Communications*, 8(6).
- [9] Rahaim, M., Miravakili, A., Borogovac, T., Little, T.D.C. and Joyner, V., 2011, September. Demonstration of a software defined visible light communication system. In the 17th Annual International Conference on Mobile Computing and Networking, *Mobicom2011*.
- [10] Rajagopal, S., Roberts, R.D. and Lim, S.K., 2012. IEEE 802.15. 7 visible light communication: modulation schemes and dimming support. *IEEE Communications Magazine*, 50(3).
- [11] Al-Hameed, A., Hussein, A.T., Alresheedi, M.T., Younus, S.H. and Elmirghani, J.M., 2017, July. Transmitters mapping of visible light communication system. In 19th International Conference on Transparent Optical Networks (ICTON 2017). IEEE.

- [12] Suzuki, N., Miura, H., Matsuda, K., Matsumoto, R. and Motoshima, K., 2018. 100 Gb/s to 1 Tb/s Based Coherent Passive Optical Network Technology. *Journal of Lightwave Technology*, 36(8), pp.1485-1491.
- [13] Wang, T.Q., Sekercioglu, Y.A., Neild, A. and Armstrong, J., 2013. Position accuracy of time-of-arrival based ranging using visible light with application in indoor localization systems. *Journal of Lightwave Technology*, 31(20), pp.3302-3308.
- [14] Eroglu, Y.S., Guvenc, I., Pala, N. and Yuksel, M., 2015, April. AOA-based localization and tracking in multi-element VLC systems. In *Wireless and Microwave Technology Conference (WAMICON), 2015 IEEE 16th Annual* (pp. 1-5). IEEE.
- [15] Guo, X., Shao, S., Ansari, N. and Khreishah, A., 2017. Indoor localization using visible light via fusion of multiple classifiers. *IEEE Photonics Journal*, 9(6), pp.1-16.
- [16] Wang, C., Yu, H.Y. and Zhu, Y.J., 2016. A long distance underwater visible light communication system with single photon avalanche diode. *IEEE Photonics Journal*, 8(5), pp.1-11.
- [17] Cheong, Y.K., Ng, X.W. and Chung, W.Y., 2013. Hazardless biomedical sensing data transmission using VLC. *IEEE sensors journal*, 13(9), pp.3347-3348.
- [18] Al-Qahtani, A., Al-hajri, H., Al-kuwari, S., Al-yaarabi, N., Al-hababi, A., Al-kubaisi, E., Ahmed, A., Kashef, M. and Abbasi, Q.H., 2015, May. A non-invasive remote health monitoring system using visible light communication. In *Future Information and Communication Technologies for Ubiquitous HealthCare (Ubi-HealthTech), 2015 2nd International Symposium on* (pp. 1-3). IEEE.
- [19] Jerlov, N.G., 2014. *Optical oceanography* (Vol. 5). Elsevier.
- [20] McConnell, P. and Adams, B., Joule Microsystems Canada Inc, 2006. Optical system and use thereof for detecting patterns in biological tissue. U.S. Patent Application 10/527,857.
- [21] Milman, J. and Halkias, C.C., 1972. *Integrated electronics*. New York.
- [22] Ghassemlooy, Z., Popoola, W. and Rajbhandari, S., 2012. *Optical wireless communications: system and channel modelling with Matlab®*. CRC press.
- [23] Clark, J. and Lanzani, G., 2010. Organic photonics for communications. *Nature photonics*, 4(7), p.438.
- [24] Ma, H., Lampe, L. and Hranilovic, S., 2013, March. Integration of indoor visible light and power line communication systems. In *Power Line Communications and Its Applications (ISPLC), 2013 17th IEEE International Symposium on* (pp. 291-296). IEEE.

- [25] Chow, C.W., Yeh, C.H., Liu, Y.F., Huang, P.Y. and Liu, Y., 2013. Adaptive scheme for maintaining the performance of the in-home white-LED visible light wireless communications using OFDM. *Optics Communications*, 292, pp.49-52.
- [26] Roberts, R.D., Rajagopal, S. and Lim, S.K., 2011, December. IEEE 802.15.7 physical layer summary. In *GLOBECOM Workshops (GC Wkshps)*, 2011 IEEE (pp. 772-776). IEEE.
- [27] Du, C., Huang, X., Jiang, C., Pu, X., Zhao, Z., Jing, L., Hu, W. and Wang, Z.L., 2016. Tuning carrier lifetime in InGaN/GaN LEDs via strain compensation for high-speed visible light communication. *Scientific reports*, 6, p.37132.
- [28] Sukhdeo, D.S., Gupta, S., Saraswat, K.C., Dutt, B.R. and Nam, D., 2016. Impact of minority carrier lifetime on the performance of strained germanium light sources. *Optics Communications*, 364, pp.233-237.
- [29] Schubert, E.F., 2018. *Light-emitting diodes*. E. Fred Schubert.
- [30] Khalid, A.M., Cossu, G., Corsini, R., Choudhury, P. and Ciaramella, E., 2012. 1-Gb/s transmission over a phosphorescent white LED by using rate-adaptive discrete multitone modulation. *IEEE Photonics Journal*, 4(5), pp.1465-1473.
- [31] Ahluwalia, G., 2008. *Cosmetics Applications of Laser and Light-Based Systems*. William Andrew.
- [32] DeLange, O.E., 1968. Optical heterodyne detection. *IEEE spectrum*, 5(10), pp.77-85.
- [33] Khalighi, M.A. and Uysal, M., 2014. Survey on free space optical communication: A communication theory perspective. *IEEE communications surveys & tutorials*, 16(4), pp.2231-2258.
- [34] Kahn, J.M. and Barry, J.R., 1997. Wireless infrared communications. *Proceedings of the IEEE*, 85(2), pp.265-298.
- [35] Kahn, J.M., You, R., Djahani, P., Weisbin, A.G., Teik, B.K. and Tang, A., 1998. Imaging diversity receivers for high-speed infrared wireless communication. *IEEE Communications Magazine*, 36(12), pp.88-94.
- [36] Zeng, L., O'Brien, D.C., Le Minh, H., Faulkner, G.E., Lee, K., Jung, D., Oh, Y. and Won, E.T., 2009. High data rate multiple input multiple output (MIMO) optical wireless communications using white LED lighting. *IEEE Journal on Selected Areas in Communications*, 27(9).
- [37] Khalighi, M.A. and Uysal, M., 2014. Survey on free space optical communication: A communication theory perspective. *IEEE communications surveys & tutorials*, 16(4), pp.2231-2258.

- [38] Ooi, V.S.Y., 2007. Intensity Modulation Direct Detection for Generating Microwave Signal in Radio Over Fiber (Doctoral dissertation, Universiti Teknologi Malaysia).
- [39] Le Minh, H., O'Brien, D., Faulkner, G., Zeng, L., Lee, K., Jung, D. and Oh, Y., 2008, September. 80 Mbit/s visible light communications using pre-equalized white LED. In Optical Communication, 2008. ECOC 2008. 34th European Conference on (pp. 1-2). IEEE.
- [40] Yun, G. and Kavehrad, M., 1993. Indoor infrared wireless communications using spot diffusing and fly-eye receivers. Canadian Journal of Electrical and Computer Engineering, 18(4), pp.151-157.
- [41] Vasilescu, I., Kotay, K., Rus, D., Dunbabin, M. and Corke, P., 2005, November. Data collection, storage, and retrieval with an underwater sensor network. In Proceedings of the 3rd international conference on Embedded networked sensor systems (pp. 154-165). ACM.
- [42] Wang, C., Yu, H.Y. and Zhu, Y.J., 2016. A long distance underwater visible light communication system with single photon avalanche diode. IEEE Photonics Journal, 8(5), pp.1-11.
- [43] Duntley, S.Q., 1963. Light in the sea. JOSA, 53(2), pp.214-233.
- [44] Woodward, B. and Sari, H., 2008. Underwater speech communications with a modulated laser. Applied Physics B, 91(1), pp.189-194.
- [45] Wang, Z., Wang, L., Zhang, Y.T. and Chen, X.D., 2009, June. *Monte carlo* simulation of light propagation in human tissue models. In Bioinformatics and Biomedical Engineering, 2009. ICBBE 2009. 3rd International Conference on (pp. 1-4). IEEE.
- [46] Xing-dan, C.H.E.N., 2008. Possibility of noninvasive clinical biochemical examination by near infrared spectroscopy [J]. Optics and Precision Engineering, 5, p.000.
- [47] Smith, A.M., Mancini, M.C. and Nie, S., 2009. Bioimaging: second window for in vivo imaging. Nature nanotechnology, 4(11), p.710.
- [48] Wang, L.V. and Wu, H.I., 2012. Biomedical optics: principles and imaging. John Wiley & Sons. [BOOK]
- [49] Niemz, M.H., 2013. Laser-tissue interactions: fundamentals and applications. Springer Science & Business Media.
- [50] Chandrasekhar, S. and Transfer, R., 1960. Dover publications. New York.
- [51] Gramatikov, B., 2012. " Handbook of biomedical optics", edited by David A. Boas, Constantinos Pitris, and Nimmi Ramanujam. [BOOK]



- [52] Ishimaru, A., 1978. Wave propagation and scattering in random media. Academ. Press.
- [53] Wang, L.V., 2009. Multiscale photoacoustic microscopy and computed tomography. *Nature photonics*, 3(9), p.503.
- [54] Wang, L., Jacques, S.L. and Zheng, L., 1995. MCML—*Monte Carlo* modeling of light transport in multi-layered tissues. *Computer methods and programs in biomedicine*, 47(2), pp.131-146.
- [55] Royston, D.D., Poston, R.S. and Prahl, S.A., 1996. Optical properties of scattering and absorbing materials used in the development of optical phantoms at 1064 nm. *Journal of biomedical optics*, 1(1), pp.110-117.
- [56] Jacques, S.L., 1998. Skin Optics. Oregon medical laser center news. (available at <https://omlc.org/software/mc>)
- [57] Shi, L., Sordillo, L.A., Rodríguez- Contreras, A. and Alfano, R., 2016. Transmission in near- infrared optical windows for deep brain imaging. *Journal of biophotonics*, 9(1-2), pp.38-43.
- [58] Hong, G., Lee, J.C., Robinson, J.T., Raaz, U., Xie, L., Huang, N.F., Cooke, J.P. and Dai, H., 2012. Multifunctional in vivo vascular imaging using near-infrared II fluorescence. *Nature medicine*, 18(12), p.1841.
- [59] Kasap, S.O. and Sinha, R.K., 2001. Optoelectronics and photonics: principles and practices (Vol. 340). New Jersey: Prentice Hall.
- [60] Wang, L., Jacques, S.L. and Zheng, L., 1995. MCML—*Monte Carlo* modeling of light transport in multi-layered tissues. *Computer methods and programs in biomedicine*, 47(2), pp.131-146.
- [61] Ahluwalia, G., 2008. *Cosmetics Applications of Laser and Light-Based Systems*. William Andrew.
- [62] Doronin, A. and Meglinski, I., 2011, February. *Monte Carlo* simulation of photon migration in turbid random media based on the object-oriented programming paradigm. In *Biomedical Applications of Light Scattering V* (Vol. 7907, p. 790709). International Society for Optics and Photonics.
- [63] Doronin, A. and Meglinski, I., 2012. Peer-to-peer *Monte Carlo* simulation of photon migration in topical applications of biomedical optics. *Journal of Biomedical Optics*, 17(9), p.090504.
- [64] [www.Biophotonics.fi](http://www.Biophotonics.fi)
- [65] Meglinski, I.V., 2001. Modeling the reflectance spectra of the optical radiation for random inhomogeneous multi-layered highly scattering and absorbing media by the *Monte Carlo* technique. *Quantum Electron*, 31(12), pp.1101-1107.

- [66] Meglinski, I.V. and Matcher, S.J., 2003. Computer simulation of the skin reflectance spectra. *Computer methods and programs in biomedicine*, 70(2), pp.179-186.
- [67] Petrov, G.I., Doronin, A., Whelan, H.T., Meglinski, I. and Yakovlev, V.V., 2012. Human tissue colour as viewed in high dynamic range optical spectral transmission measurements. *Biomedical optics express*, 3(9), pp.2154-2161.
- [68] Chen, Chia-Wei, et al. "Visible light communications for the implementation of internet-of-things." *Optical Engineering* 55.6 (2016): 060501.
- [69] Kadam, Krishna, and Manisha R. Dhage. "Visible light communication for IoT." 2016 2nd International Conference on Applied and Theoretical Computing and Communication Technology (iCATccT) . IEEE, 2016.
- [70] Böcker, Adam, et al. "An implementation of a visible light communication system." Bachelor thesis, Chalmers University of Technology-Gothenburg, Sweden (2015).
- [71] Feng, Zi, et al. "Performance of visible light communications with dimming controls." 2014 IEEE Wireless Communications and Networking Conference (WCNC) . IEEE, 2014.
- [72] Sarbazi, Elham, and Murat Uysal. "PHY layer performance evaluation of the IEEE 802.15 .7 visible light communication standard." 2013 2nd International workshop on optical wireless communications (IWOW) . IEEE, 2013.
- [73] Matcher, SJ, et al. "Performance comparison of several published tissues near-infrared spectroscopy algorithms." *Analytical Biochemistry* 227.1 (1995): 54-68.

## **8. APPENDICES**

Appendix 1. MCXYZ.m

Appendix 2. BIOPHOTONICS.m

## Appendix 1. MCXYZ.m

```

%% Original Script: (lookmcxyz.m) Steven L Jacques
% Revision: Date 01:06:2018
% Modified by: Syed Isphandiyar Ali
% This script calculates bitrate in biological tissue at 633 nm
using the
% optical properties of tissue model given in the following
references.

%% Reference
% Jacques, S.L. and Li, T., 2013. Monte Carlo simulations of light
% transport in 3D heterogenous tissues (mcxyz. c). See
http://omlc.
% org/software/mc/mcxyz/index.

home; clear
format compact
commandwindow

SAVEPICSON = 1;
if SAVEPICSON
    sz = 10; fz = 7; fz2 = 5; % to use savepic.m
else
    sz = 12; fz = 9; fz2 = 7; % for screen display
end
%%% USER CHOICES <----- you must specify -----
myname = 'skinvessel'; nm = 770;
%%%

disp(sprintf('----- mcxyz %s -----',myname))

% Load header file
filename = sprintf('%s_H.mci',myname);
disp(['loading ' filename])
fid = fopen(filename, 'r');
A = fscanf(fid, '%f', [1 Inf]);
fclose(fid);

%% parameters
time_min = A(1);
Nx = A(2);
Ny = A(3);
Nz = A(4);
dx = A(5);
dy = A(6);
dz = A(7);
mcflag = A(8);
launchflag = A(9);
boundaryflag = A(10);
xs = A(11);
ys = A(12);
zs = A(13);
xfocus = A(14);
yfocus = A(15);
zfocus = A(16);
ux0 = A(17);
uy0 = A(18);

```

```

uz0 = A(19);
radius = A(20);
waist = A(21);
Nt = A(22);
j = 22;
for i=1:Nt
    j=j+1;
    muav(i,1) = A(j);
    j=j+1;
    musv(i,1) = A(j);
    j=j+1;
    gv(i,1) = A(j);
end

reportHmci(myname)

%% Load Fluence rate F(y,x,z)
filename = sprintf('%s_F.bin',myname);
disp(['loading ' filename])
tic
    fid = fopen(filename, 'rb');
    [Data count] = fread(fid, Ny*Nx*Nz, 'float');
    fclose(fid);
toc
F = reshape(Data,Ny,Nx,Nz); % F(y,x,z)

%%
% Load tissue structure in voxels, T(y,x,z)
filename = sprintf('%s_T.bin',myname);
disp(['loading ' filename])
tic
    fid = fopen(filename, 'rb');
    [Data count] = fread(fid, Ny*Nx*Nz, 'uint8');
    fclose(fid);
toc
T = reshape(Data,Ny,Nx,Nz); % T(y,x,z)

clear Data

%%
x = ([1:Nx]-Nx/2-1/2)*dx;
y = ([1:Ny]-Ny/2-1/2)*dx;
z = ([1:Nz]-1/2)*dz;
ux = [2:Nx-1];
uy = [2:Ny-1];
uz = [2:Nz-1];
zmin = min(z);
zmax = max(z);
zdiff = zmax-zmin;
xmin = min(x);
xmax = max(x);
xdiff = xmax-xmin;

%% Look at structure, Tzx
Tzx = reshape(T(Ny/2, :, :), Nx, Nz)';
tissue = makeTissueList(nm);
Nt = length(tissue);

figure();clf

```

```

imagesc(x(ux),z(uz),Tzx(uz,ux),[1 Nt])
hold on
cmap = makecmap(Nt);
colourmap(cmap)
colourbar
set(gca,'fontsize',sz)
set(colourbar,'fontsize',1)
xlabel('x [cm]')
ylabel('z [cm]')
title('Tissue','fontweight','normal','fontsize',fz2)
for i=1:Nt
    yy = zmin + (Nt-i)/(Nt-1)*zdiff;
    text(xmax*1.4,yy, sprintf('%d
%s',i,tissue(i).name),'fontsize',fz2)
end

% draw launch
N = 20; % # of beam rays drawn
switch mcflag
    case 0 % uniform
        for i=0:N
            plot((-radius + 2*radius*i/N)*[1 1],[zs max(z)],'r-')
        end

    case 1 % Gaussian
        for i=0:N
            plot([(-radius + 2*radius*i/N) xfocus],[zs zfocus],'r-
')
        end

    case 2 % iso-point
        for i=1:N
            th = (i-1)/19*2*pi;
            xx = Nx/2*cos(th) + xs;
            zz = Nx/2*sin(th) + zs;
            plot([xs xx],[zs zz],'r-')
        end

    case 3 % rectangle
        zz = max(z);
        for i=0:N
            xx = -radius + 2*radius*i/N;
            plot([xx xx],[zs zz],'r-')
        end
end
axis equal image

if SAVEPICSON
    name = sprintf('%s_tissue.jpg',myname);
    savepic(1,[4 3],name)
end

%% Look at Fluence Fzx @ launch point
Fzx = reshape(F(Ny/2, :, :),Nx,Nz)'; % in z,x plane through source

figure();clf
imagesc(x,z,log10(Fzx),[.5 2.8])
hold on

```

```

    text(max(x)*1.2,min(z)-0.04*max(z),'log_{10}( \phi
)','fontsize',fz)
    colourbar
    set(gca,'fontsize',sz)
    xlabel('x [cm]')
    ylabel('z [cm]')
    title('Fluence \phi [W/cm^2/W.delivered]
','fontweight','normal','fontsize',fz)
    colourmap(makec2f)
    axis equal image
    %axis([min(x) max(x) min(z) max(z)])
    text(min(x)-0.2*max(x),min(z)-0.08*max(z),sprintf('runtime = %0.1f
min',time_min),...
        'fontsize',fz2)

    if SAVEPICSON
        name = sprintf('%s_Fzx.jpg',myname);
        savepic(2,[4 3],name)
    end

    %% look Fzy
    Fzy = reshape(F(:,Nx/2,:),Ny,Nz)';

    iy = round((dy*Ny/2 + 0.15)/dy);
    iz = round(zs/dz);
    zzs = zs;
    %Fdet = mean(reshape(Fzy(iz+[-1:1],iy+[0 1]),6,1));

    figure();clf
    imagesc(y,z,log10(Fzy),[.5 2.8])
    hold on
    text(max(x)*1.2,min(z)-0.04*max(z),'log_{10}( \phi
)','fontsize',fz)
    colourbar
    set(gca,'fontsize',sz)
    xlabel('y [cm]')
    ylabel('z [cm]')
    title('Fluence \phi [W/cm^2/W.delivered]
','fontweight','normal','fontsize',fz)
    colourmap(makec2f)
    axis equal image
    text(min(x)-0.2*max(x),min(z)-0.08*max(z),sprintf('runtime = %0.1f
min',time_min),...
        'fontsize',fz2)

    if SAVEPICSON
        name = sprintf('%s_Fzy.jpg',myname);
        savepic(3,[4 3],name)
    end

    %% look Azx
    Fzx = reshape(F(Ny/2,:),Nx,Nz)'; % in z,x plane through source
    mua = muav(reshape(T(Ny/2,:),Nx,Nz)');
    Azx = Fzx.*mua;

    figure();clf
    imagesc(x,z,log10(Azx))
    hold on
    text(max(x)*1.2,min(z)-0.04*max(z),'log_{10}( A )','fontsize',fz)

```

```

colourbar
set(gca,'fontsize',sz)
xlabel('x [cm]')
ylabel('z [cm]')
title('Fluence Rate A [W/cm^3/W.delivered]
','fontweight','normal','fontsize',fz)
colourmap(makec2f)
axis equal image
%axis([min(x) max(x) min(z) max(z)])
text(min(x)-0.2*max(x),min(z)-0.08*max(z),sprintf('runtime = %0.1f
min',time_min),...
      'fontsize',fz2)

if SAVEPICSON
    name = sprintf('%s_Azx.jpg',myname);
    savepic(2,[4 3],name)
end

drawnow

disp('done')

%%modification start
Rx_Area = 0.2300; % xxPhotodiode active area mm^2
Ra = 0.46; % Responsivity
q = 1.602e-19; % electron charge
Id = 10e-9; % xxPhotodiode dark current
T = 300; % Temperature
K = 1.38*10^-23; % Boltzman constant
R = 1; % [Ohms] Resistance of Circuitry
BW = 100e3; % Bandwidth
%% Bit Rate Calculations
% Incident optical Intensity W/mm^2
image=Azx;
Fluence_Rate = (image(:,100));
ps = 10^-12;
tau_d=[];
for i =1:200
    tau_d = [tau_d, i*ps];
end
Intensity = Fluence_Rate ./ tau_d;
P_r = Intensity*Rx_Area; % Received optical power
I_ph = Ra*P_r; % Photocurrent
i_shot = sqrt(2*q*I_ph*BW); % Shot Noise
i_johnson = (4*K*T*BW)/R; % Johnson Noise
i_tot_noise = sqrt((Id^2)+(i_shot.^2)+(i_johnson^2)); % Total
Noise
SNR = (I_ph.^2)./(i_tot_noise.^2); % Signal to
noise_ratio
C = (BW*(log2(1+SNR)))/10^6; % Shannon Achievable Capacity in
Mbps
% Plot (Tissue depth vs bitrate [Mbps])

figure()

plot(z,log10(C(:,100)))
hold on
text(max(x)*1.2,min(z)-0.04*max(z),'log_{10}( A )','fontsize',fz)
set(gca,'fontsize',sz)

```



```

xlabel('x [cm]')
ylabel('z [cm]')
title('Fluence Rate A [W/cm^3/W.delivered]
', 'fontweight', 'normal', 'fontsize', fz)
colourmap(makec2f)
axis equal image
text(min(x)-0.2*max(x), min(z)-0.08*max(z), sprintf('runtime = %0.1f
min', time_min), ...
      'fontsize', fz2)
xlabel('depth [cm]')
ylabel('Shannon Capacity - Mbps ')
set(gca, 'FontSize', 14)
grid on;
title('Tissue depth vs bitrate [Mbps]')
%%modification end

```

## Appendix 2. BIOPHOTONICS.m

```

%% Original Script: (biophotonics.m) Ali Asphandiyar
% Date 01:06:2018
% This script calculates bitrate in biological tissue at 633 nm
using the
% optical properties of tissue model given in the following
references.

%% Reference 1
% A.V. Doronin, I.V. Meglinski, "Peer-to-Peer Monte
% Carlo simulation of photon migration in topical applications of
% biomedical optics", Journal of Biomedical Optics, Vol. 17, Issue
9, 090504 (2012)

%% Reference 2
% A.V. Doronin, I.V. Meglinski, "Online Object-Oriented Monte
Carlo
% computational tool for the needs of biomedical optics",
% Biomedical Optics Express, Vol. 2, Issue 9, pp.2461-2469 (2011)

%% Given Inputs
Clear; % clear work space
close all; % closes all the open figure windows
clc; % Clear command window
tissue_dep = [0:(5/100):5-0.01]; % Tissue Depth
Rx_Area = 0.2300; % Photodiode active area mm^2
Ra = 0.46; % Responsivity
q = 1.602e-19; % electron charge
Id = 10e-9; % Photodiode dark current
T = 300; % Temperature
K = 1.38*10^-23; % Boltzmann constant
R = 1; % [Ohms] Resistance of Circuitry
BW = 100e3; % Bandwidth

%% Bit Rate Calculations
% Incident optical Intensity W/mm^2
image=load('08022018123632_arz.flrt');
Fluence_Rate = image(1:100);
ps = 10^-12;
tau_d=[];
for i =1:100
tau_d = [tau_d, i*ps];
end
Intensity = Fluence_Rate ./ tau_d;
P_r = Intensity*Rx_Area; % Received optical power
I_ph = Ra*P_r; % Photocurrent
i_shot = sqrt(2*q*I_ph*BW); % Shot Noise
i_johnson = (4*K*T*BW)/R; % Johnson Noise
i_tot_noise = sqrt((Id^2)+(i_shot.^2)+(i_johnson^2)); % Total
Noise
SNR = (I_ph.^2)./(i_tot_noise.^2); % Signal to noise ratio
C = (BW*(log2(1+SNR)))/10^6; % Shannon Achievable Capacity in
Mbps
%% Plot (Tissue depth vs bitrate [Mbps])
figure;
plot(tissue_dep,C,'--ks','LineWidth',2,...
'MarkerEdgeColour','r',...
'MarkerFaceColour','g',...

```

```

'MarkerSize',10)

xlabel('depth [mm]')
xlim([min(tissue_dep) max(tissue_dep)])
ylabel('Shannon Capacity - Mbps ')
set(gca,'FontSize',14)
grid on;
title('Tissue depth vs bitrate [Mbps]')
figure()
plot(tissue_dep,log10(C))
xlabel('depth [mm]')
ylabel('Shannon Capacity - Mbps ')
set(gca,'FontSize',14)
grid on;
title('Tissue depth vs bitrate [Mbps]')

```